Rest-frame electrodynamics and polarizability theory for rotating two-dimensional structures and particle arrays

Ido Kazma, Tomer Geva, and Ben Z. Steinberg*
School of Electrical Engineering, Tel-Aviv University, Tel Aviv-Yafo, 6997801, Israel

(Received 10 August 2023; revised 20 June 2024; accepted 24 June 2024; published 11 July 2024)

An electrodynamic (ED) theory for 2D particle arrays that undergo a slow rigid rotation $\mathbf{\Omega}$ and observed in their rest frame of reference $\mathcal{R}^{\Omega}$ is developed. The theory holds for both transverse electric (TE) and transverse magnetic (TM) excitations. Analytical and numerical techniques are applied, in conjunction of a suitable Greens function, to study the effect of rotation on electrically small 2D scatterers such as dielectric cylinders of arbitrary isotropic material and cross-section geometry, and to derive the polarizability matrix in $\mathcal{R}^{\Omega}$ and the corresponding discrete dipole formulation. The formulation is then used for a preliminary study of particle arrays and tested against full wave numerical solutions of rotating structures that hold in $\mathcal{R}^{\Omega}$. The basic physical mechanisms that govern the rotation footprint on the array response are explored and discussed, and their ramifications on TE and TM cases are contrasted. These mechanisms hold in general and are not idiosyncratic to 2D. It is shown that the ED is mainly due to the excitation of a large number of Sagnac loops created inside the structure as a result of the multiple scattering events between the array inclusions. However, the collective interactions of a large number of loop exhibit a net dynamics that is far more intricate than that of a single Sagnac loop, and even contradicts it in some aspects. The rotation footprint on the collective ED properties of a 2D periodic structure such as stop-band location, induced nonreciprocity, and the role of the structure symmetries in these effects are explored.

DOI: 10.1103/PhysRevB.110.035129

I. INTRODUCTION

The electrodynamics (ED) of moving, accelerating, or rotating structures and particle arrays supports unique effects of light-matter interaction such as dynamically controlled bianisotropy and nonreciprocity [1–3], vacuum-friction [4], and gain and instabilities [5–7]. These may potentially serve as platforms for new technologies and applications such as isolators and circulators, energy harvesting devices, rotation sensors, and more. Of particular interest is the case of structures rotating at a given angular velocity $\mathbf{\Omega}$, as rotation is inherently noninertial, thus it exhibits a wide class of unique physical phenomena. Furthermore, compared to linear translation, rotation can be manifested in smaller physical settings. The ED of rotating structures as observed in the laboratory (inertial) frame of reference has been investigated extensively. Pioneering studies can be found, e.g., in Refs. [5,8–11], dealing with structures that are large compare to the electromagnetic wavelength λ, with interest mainly in the far-field scattering. However, advances in fabrication technologies, photonic crystals, microcavities, and metamaterials in the last decades have spurred the interest in rotating nanoparticles and microstructures whose electrical dimensions are small with respect to the wavelength λ, or λ-comparable, with much larger rotation rates; experiments achieving mechanical rotation exceeding 1 GHz were reported [12,13]. Theoretical studies of rotating photonic crystals and microcavities [14,15] have shown the manifestation of the fundamental Sagnac effect [16] in nontrivial structures where the electromagnetic field cannot be described as a mere ray-optical light wave. The roles of mode degeneracy and symmetry in the Sagnac effect, with applications to rotation sensing were explored in Refs. [15,17–20]. Dichroism of rotating particles, in response to the special excitation of impinging wave of circular polarization and the corresponding *scalar* polarizability have been explored in Ref. [21].

One way to classify the analytical approaches of the studies mentions above is the *frame of reference* (FoR) used for the governing theoretical formulation. At first glance the laboratory *inertial* FoR $\mathcal{R}_I$ may seem to be a natural choice. However, if the system possesses a complex nonsymmetrical structure with arbitrary rotation axis, then the analysis in $\mathcal{R}_I$ may become insurmountable, merely by the fact that one needs to follow complex time-dependent geometries and boundaries. Indeed, most of the studies above that were formulated in $\mathcal{R}_I$ are limited to highly symmetric particles—bodies of revolution—rotating around their own symmetry axis, thus alleviating the need to deal with time-dependent geometries. The challenges associated with bodies of richer inner structure or boundaries *rigidly* rotating around an arbitrary axis at the angular velocity $\mathbf{\Omega}$, is more conveniently addressed by formulating the problem in the rotating structure *rest* FoR $\mathcal{R}^{\Omega}$. This approach is invoked in Refs. [7,14,15,17–20], where microstructures of arbitrary shape and rotation axis were studied. We note that there is a class of important applications that is naturally suitable for analysis in $\mathcal{R}^{\Omega}$—namely optical gyroscopes and inertial navigation systems, in

*Contact author: steinber@eng.tau.ac.il

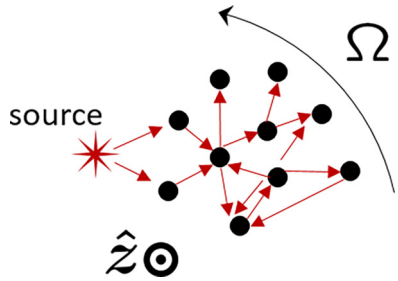

FIG. 1. A 2D particle array of arbitrary geometry, and a source that excites it, rotate rigidly at an angular velocity $\boldsymbol{\Omega} = \hat{z}\Omega$. It consists of electrically small dielectric scatterers located at an arbitrary distances from the rotation axis z. The structure is observed in its rest frame of reference (FoR) $\mathcal{R}^{\Omega}$. We study the structure ED in $\mathcal{R}^{\Omega}$.

which both the structure excitation and response measurement are executed in the rotating platform. Furthermore, even if the rotating system is intended to be excited and measured by a source and/or an observer that are stationary in $\mathcal{R}_I$, the transformation of the incident/scattered field from $\mathcal{R}_I$ to $\mathcal{R}^{\Omega}$ and back can be done using standard explicit expressions [22], while the significantly more difficult task of solving the scattering problem itself—the heart of the matter—still can be done in $\mathcal{R}^{\Omega}$ where it possesses static boundaries. We note that the transformations $\mathcal{R}_I \to \mathcal{R}^{\Omega} \to \mathcal{R}_I$ may generate a set of higher harmonics; then our formulation can be applied to each of these harmonics independently, and sum up the results.

The goal of the present study is to develop a framework governing the ED of two-dimensional structures and particle arrays that undergo slow rigid rotation, in their rest FoR $\mathcal{R}^{\Omega}$, as shown schematically in Fig. 1. The structures consist of arbitrary arrays of 2D dielectric microscatterers of arbitrary cross section geometry, with arbitrary location of the rotation axis. The incident fields or sources that excite the structure, and the observation points, are all defined in $\mathcal{R}^{\Omega}$. Thus, for example, a point-source excitation corresponds to the field due to a point source that rotates together with the structure. We approach the problem via two routes. One is purely numerical, in which an *exact* solution for the scatterers polarization currents is achieved. While this approach is robust, it becomes impractical when the number of scatterers is very large. The second route is based on the polarizability theory and discrete dipole approximation adopted to hold in $\mathcal{R}^{\Omega}$. First, the polarizability matrix of an individual scatter is investigated both numerically and analytically, and its dependence on $\boldsymbol{\Omega}$ and on the distance from the rotation axis, is explored. Then, it is used to formulate a discrete dipole approximation (DDA) governing the response of an entire arbitrary array under rigid rotation, in $\mathcal{R}^{\Omega}$. This approach can handle the rotation of arrays consisting of a very large number of scatterers. A critical comparison between these two routes, and the ensuing study of these structures, reveal the physical mechanisms underlying the rotation-induced effects and their footprint on the structure response. We define this response as the polarization currents $\boldsymbol{I}_n, n = 1, \ldots N$ excited in the $N \gg 1$ electrically small inclusions consisting the structure. Specifically, we observe that

(1) The rotation footprint on the response is dominated by the interferences of the large number of Sagnac loops created by the multiple scattering events between the inclusions.

(2) The response magnitudes $|\boldsymbol{I}_n|$ may possess an intricate nonmonotonic dependence on Ω. However, these magnitudes are independent of the location of the rotation axis.

(3) The phases of $\boldsymbol{I}_n, n = 1, \ldots N$ incorporate information about the distance from the rotation axis through a linear relationship. This is unlike the conventional Sagnac effect where this information is not available at all.

(4) The sensitivity of the particle array response to rotation depends on the background material. This effect even contradicts the classical Sagnac effect that is known to be independent of the background material [16]. It is attributed to the multiplicity of independent and yet interfering Sganac loops.

(5) The collective properties of periodic structures such as the frequency stop-band and the resulting optical transmission, become nonreciprocal. The effect of rotation on these properties—in particular on the nonreciprocity manifestation—depends on the structure' geometrical symmetries.

(6) The response sensitivity under transverse magnetic (TM) excitation is significantly higher than that of the transverse electric (TE) excitation.

Clearly both routes—the numerical and the semianalytical DDA—require the development of analytic infrastructure common to classical problems in applied EM, namely rigorous Greens function theory in $\mathcal{R}^{\Omega}$ and boundary conditions, and both will be discussed here. An exact spectral representation of the former has already been developed in Ref. [23]; we show below that it encapsulate the Sagnac effect, as well as the instabilities induced by rotation discussed previously within $\mathcal{R}_I$ [5,6] and $\mathcal{R}^{\Omega}$ [7,8] formulations.

II. FORMULATION

We develop a formulation governing the ED of rigidly rotating particle arrays (PA's); the entire structure rotates at an angular velocity $\boldsymbol{\Omega} = \hat{z}\Omega$ relative to the inertial frame $\mathcal{R}_I$. Here and henceforth, a bold (overhat) letter denotes a vector (a unit vector). We *define* the frame of reference $\mathcal{R}^{\Omega}$ as the system at which the structure appears at rest. The z axis of $\mathcal{R}^{\Omega}$ coincides with that of $\mathcal{R}_I$, and the coordinates in $\mathcal{R}^{\Omega}$ normal to the rotation axis are denoted by $\boldsymbol{\rho} = \hat{\boldsymbol{x}}x + \hat{\boldsymbol{y}}y = \rho\hat{\boldsymbol{\rho}}$. We always observe the ED as seen in $\mathcal{R}^{\Omega}$, and the corresponding problem is termed here as the "$\mathcal{R}^{\Omega}$ problem." The specific case of $\mathcal{R}^0$ and the "$\mathcal{R}^0$ problem" corresponds to $\Omega = 0$ indicating that both the observer and the structure are at rest in the FoR $\mathcal{R}_I$, rendering $\mathcal{R}^0$ and $\mathcal{R}_I$ the same. Since $\mathcal{R}^{\Omega}$ is noninertial for $\Omega \neq 0$, an observer at rest there sees formally curved space-time. However, it can be considered locally flat for distances D satisfying $D \ll c^2/A$ where A is the acceleration of $\mathcal{R}^{\Omega}$ and c is the speed of light in vacuum [24]. Here $A = \Omega^2 D$ that yields the slow rotation condition $\Omega D \ll c$. Our study is restricted to this regime.

We assume that the material in the corresponding $\mathcal{R}^0$ problem is characterized by the scalar permittivity $\epsilon(\boldsymbol{r}) = \epsilon_0\epsilon_r(\boldsymbol{r})$ and permeability $\mu(\boldsymbol{r}) = \mu_0\mu_r(\boldsymbol{r})$. They can possess dispersion of arbitrary form as well as resonances, such as, e.g., in plasmonic materials. Under the slow rotation condition articulated above, the $\mathcal{R}^{\Omega}$ problem is still governed by the conventional set of Maxwell equations (ME) of $\mathcal{R}^0$ problem,

where the rotation footprint is manifested only via the modified constitutive relations. Up to first order in Ω they are given by [1]

$$\boldsymbol{D} = \epsilon \boldsymbol{E} - c^{-2}(\boldsymbol{\Omega} \times \boldsymbol{r}) \times \boldsymbol{H}, \tag{1a}$$

$$\boldsymbol{B} = \mu \boldsymbol{H} + c^{-2}(\boldsymbol{\Omega} \times \boldsymbol{r}) \times \boldsymbol{E}. \tag{1b}$$

Note that the rotation footprint in $\boldsymbol{B}, \boldsymbol{D}$ is medium independent (c is the speed of light in vacuum). For homogeneous ϵ_r, μ_r and z-independent excitations the resulting set of ME can be separated into independent TE and TM fields and rigorous 2D Green's function can be obtained [23]. As shown in Appendix A it can be extended to hold for nonhomogeneous z-independent media, i.e., where $\epsilon = \epsilon(\boldsymbol{\rho})$, $\mu = \mu(\boldsymbol{\rho})$. For convenience we summarize these results below. In both polarizations the complete EM field can be obtained uniquely from a z-directed field F_z satisfying the modified scalar Helmholtz equation (time dependence $e^{-i\omega t}$ is assumed and suppressed)

$$\left(\tau \nabla_t \cdot \frac{1}{\tau} \nabla_t + k_0^2 n^2\right) F_z - i k_0^2 \bar{\Omega} \left(\partial_\theta + \tau \partial_\theta \frac{1}{\tau}\right) F_z = S, \tag{2}$$

where $\bar{\Omega} = \Omega/\omega$, $k_0 = \omega/c$, and $n^2 = \epsilon_r(\boldsymbol{\rho})\mu_r(\boldsymbol{\rho})$. In the equation above only terms that are up to first order in Ω are kept (see Appendix A).

The TE polarization consists of $H_z = F_z, \boldsymbol{E}_t = \hat{\boldsymbol{x}} E_x + \hat{\boldsymbol{y}} E_y$ with $\tau = \epsilon_r(\boldsymbol{\rho})$ and

$$i\omega \epsilon \boldsymbol{E}_t = \boldsymbol{J}_t^{\mathrm{E}} - \nabla_t \times \hat{\boldsymbol{z}} H_z + i\bar{\Omega} k_0^2 \boldsymbol{\rho} H_z \tag{3a}$$

and with the source term

$$S = S^{\mathrm{TE}} = -i\omega \epsilon J_z^{\mathrm{M}} - i\bar{\Omega} k_0^2 \boldsymbol{\rho} \cdot \boldsymbol{J}_t^{\mathrm{E}} - \hat{\boldsymbol{z}} \cdot \epsilon \nabla_t \times \frac{1}{\epsilon} \boldsymbol{J}_t^{\mathrm{E}}. \tag{3b}$$

Likewise, TM consists of $E_z = F_z, \boldsymbol{H}_t$ with $\tau = \mu_r(\boldsymbol{\rho})$ and

$$i\omega \mu \boldsymbol{H}_t = \boldsymbol{J}_t^{\mathrm{M}} + \nabla_t \times \hat{\boldsymbol{z}} E_z - i\bar{\Omega} k_0^2 \boldsymbol{\rho} E_z, \tag{4a}$$

$$S = S^{\mathrm{TM}} = -i\omega \mu J_z^{\mathrm{E}} + i\bar{\Omega} k_0^2 \boldsymbol{\rho} \cdot \boldsymbol{J}_t^{\mathrm{M}} + \hat{\boldsymbol{z}} \cdot \mu \nabla_t \times \frac{1}{\mu} \boldsymbol{J}_t^{\mathrm{M}}, \tag{4b}$$

where we have used the cylindrical system $\boldsymbol{r} = (z, \boldsymbol{\rho}) = (z, \rho, \theta)$. Clearly, for any scalar S, the fields can be obtained via a superposition integral of the scalar Green function $G^{\Omega}(\boldsymbol{\rho}, \boldsymbol{\rho}')$ defined as the impulse response of Eq. (2) with $S \mapsto -\delta(\boldsymbol{\rho} - \boldsymbol{\rho}') = \frac{-1}{\rho'} \delta(\rho - \rho') \delta(\theta - \theta')$. Note that for a thin wire electric (magnetic) current $\boldsymbol{J}^{\mathrm{E}} = \hat{\boldsymbol{z}} I_z^{\mathrm{E}} \delta(\boldsymbol{\rho} - \boldsymbol{\rho}')$ [$\boldsymbol{J}^{\mathrm{M}} = \hat{\boldsymbol{z}} I_z^{\mathrm{M}} \delta(\boldsymbol{\rho} - \boldsymbol{\rho}')$] the excited field is only of the TM (TE) polarization, with the electric (magnetic) field $E_z = i\omega \mu I_z^{\mathrm{E}} G^{\Omega}(\boldsymbol{\rho}, \boldsymbol{\rho}')$ [$H_z = i\omega \epsilon I_z^{\mathrm{M}} G^{\Omega}(\boldsymbol{\rho}, \boldsymbol{\rho}')$].

It has been shown in Ref. [23] that a complete and exact expression for G^{Ω} in a *homogeneous medium* is given by the spectral summation

$$G^{\Omega}(\boldsymbol{\rho}, \boldsymbol{\rho}') = \frac{i}{4} \sum_{m=-\infty}^{\infty} J_m(k_0 n \gamma_m \rho_<) H_m^{(1)}(k_0 n \gamma_m \rho_>) e^{im(\theta - \theta')}, \tag{5}$$

where $\gamma_m = \sqrt{1 + 2m\Omega/(\omega n^2)}$ and $\rho_{\gtrless} = \max_{\min}(\rho, \rho')$. Below we discuss some of its basic properties.

A. Nonreciprocity, rotation-induced gain, and a uniform approximation of G^{Ω}

The expansion in Eq. (5) is exact and contains the entire spectrum of the problem, meaning it encapsulates all the physical effects that can take place. For example, rotation-induced nonreciprocity is manifested by the Bessel and Hankel arguments that depend nonsymmetrically on the sign of $m\Omega$ via γ_m, leading to $G^{\Omega}(\boldsymbol{\rho}, \boldsymbol{\rho}') \neq G^{\Omega}(\boldsymbol{\rho}', \boldsymbol{\rho})$. Rotation-induced gain and instabilities are also presented. They are manifested by the spatial harmonics that satisfy $2m\Omega < -\omega n^2$, rendering γ_m imaginary and hence exponential growth of J_m and $H_m^{(1)}$. This is consistent with the observation in Refs. [5,8]. To estimate the magnitudes of the exponentially growing harmonics, assume that $\rho > \rho'$ and that $k_0 n \rho' |\gamma_m| \leqslant 1$. Then these magnitudes scale as

$$J_m(k_0 n |\gamma_m| \rho') \simeq \frac{(k_0 n |\gamma_m| \rho')^{|m|}}{2^{|m|} |m|!}. \tag{6}$$

For applications in the optical frequencies (e.g., $\lambda = 1$ μm) this number practically vanishes; even if Ω is in the GHz domain, we get $|m| = \mathcal{O}(10^6)$. Thus, rotation-induced gain in 2D optical PA of finite spatial extent is extremely hard to observe. Note, however, that in the limit of low ω and 3D structures operating in the quasistatic limit, such gain and instabilities may be less difficult to observe. This is studied in Ref. [7].

Finally, note that the rotation footprint in G^{Ω} vanishes if the source is located exactly at the rotation axis, i.e., if $\rho' = 0$. In this case Eq. (5) reduces to the celebrated 2D Green function for $\mathcal{R}^0$ problem. This does not mean, however, that the rotation has no effect on the *fields*; Ω is still present in $\boldsymbol{E}_t$ ($\boldsymbol{H}_t$) for TE (TM) polarization, as seen in Eq. (3a) [Eq. (4a)].

The presentation of G^{Ω} in Eq. (5) has several practical drawbacks. First, $G^{\Omega}(\boldsymbol{\rho}, \boldsymbol{\rho}')$ diverges logarithmically as $\boldsymbol{\rho} \to \boldsymbol{\rho}'$ (as any Greens function of a 2D PDE). This singular behavior is not present in each of the summed terms above (unless $\rho' = 0$). Thus, in the near fields as $\boldsymbol{\rho} \to \boldsymbol{\rho}'$ the series converges very slow. The second difficulty stems from the fact that we are interested not only in near fields, but also in far-field behavior to accommodate for nonlocal interactions between remote particles. This requires the evaluation of J_m, $H_m^{(1)}$ for large argument and order, that is also quite difficult to attain in sufficient accuracy. In light of these issues, and recalling that the spatial harmonics representing the rotation-induced gain in the optical frequencies correspond to extremely large m and is impractical here, one may limit m. Thus, we approximate $\gamma_m \simeq 1 + m\Omega/(n^2\omega)$, that for practical values of Ω/ω still holds for a large range of m, and apply the addition theorem. This procedure was invoked in Ref. [23], and it yields

$$G^{\Omega}(\boldsymbol{\rho}, \boldsymbol{\rho}') = G^0(\boldsymbol{\rho}, \boldsymbol{\rho}') e^{ik_0^2 \bar{\Omega} \hat{\boldsymbol{z}} \cdot (\boldsymbol{\rho}' \times \boldsymbol{\rho})}, \tag{7a}$$

where

$$G^0(\boldsymbol{\rho}, \boldsymbol{\rho}') = G^{\mathrm{ST}}(\boldsymbol{\rho}, \boldsymbol{\rho}') = \frac{i}{4} H_0^{(1)}(k_0 n |\boldsymbol{\rho} - \boldsymbol{\rho}'|) \tag{7b}$$

G^{ST} is the Green's function of the $\mathcal{R}^0$ problem. Note that the singularity of G^{Ω} as $\boldsymbol{\rho} \to \boldsymbol{\rho}'$ is fully encapsulated in G^{ST}, since the other term is regular in this limit. This is quite expected since both the stationary and rotating medium Green's

functions satisfy a PDE that possesses exactly the same form of the higher (second-order) derivatives—see Eq. (2)—and therefore must have the same singularity. Despite its simplicity, this expression provides a good approximation for the rotating medium Green's function. A detailed comparison is performed in Refs. [23,25]. Furthermore, note that the rotation footprint in Eq. (7a) is present only in the exponent that is medium-independent, and the exponential term $\hat{\boldsymbol{z}}\cdot(\boldsymbol{\rho}'\times\boldsymbol{\rho})$ is nothing but twice the area of the triangle whose vertexes are $\boldsymbol{\rho}$, $\boldsymbol{\rho}'$ and the origin. Thus, this term eventually provides the Sagnac effect [25]. In fact, Eq. (7a) is a uniform approximation of the exact expression in Eq. (5) as $\Omega/\omega\to 0$, valid from near to far fields, and it excludes only the rotation-induced instability. This Green function is used throughout the rest of this work.

Finally note the inversion, shift, and mirroring properties of both the exact and the approximated G^{Ω} in Eq. (5) and Eqs. (7a) and (7b).

Inversion:

$$G^{\Omega}(\boldsymbol{\rho},\boldsymbol{\rho}')=G^{-\Omega}(\boldsymbol{\rho}',\boldsymbol{\rho}) \tag{8a}$$

that is equivalent to inversion of rotation.

Shift:

$$G^{\Omega}(\boldsymbol{\rho}-\boldsymbol{\rho}_0,\boldsymbol{\rho}'-\boldsymbol{\rho}_0)=G^{\Omega}(\boldsymbol{\rho},\boldsymbol{\rho}')e^{ik_0^2\bar{\Omega}\hat{\boldsymbol{z}}\cdot[\boldsymbol{\rho}_0\times(\boldsymbol{\rho}'-\boldsymbol{\rho})]}. \tag{8b}$$

Mirroring: Let $\tilde{\boldsymbol{\rho}}$ be the mirroring of $\boldsymbol{\rho}$ over a line that passes though the origin (=rotation axis) at angle θ. We have $\tilde{\boldsymbol{\rho}}=M_\theta\boldsymbol{\rho}$ with $M_{11}=-M_{22}=\cos 2\theta$, $M_{12}=M_{21}=\sin 2\theta$, $\forall\,\theta$. Then

$$G^{\Omega}(\tilde{\boldsymbol{\rho}},\tilde{\boldsymbol{\rho}}')=G^{-\Omega}(\boldsymbol{\rho},\boldsymbol{\rho}') \tag{8c}$$

that again is equivalent to inversion of rotation. The proof of this identity is straightforward; under mirroring G^0 is invariant, while $\boldsymbol{\rho}'\times\boldsymbol{\rho}$ merely changes sign. Likewise, the proof for G^{Ω} in Eq. (5) is easily obtained by observing that the operator M_ϕ leaves ρ, ρ' unchanged, but reverses the sign of $\theta-\theta'$. These relations are used below to deduce symmetry properties of the ED of particle arrays.

B. Green's Dyad

For infinitesimal current sources, the formulation in Eqs. (3a)–(5) can be wrapped in a compact form via the Green function dyad $\mathbb{G}^{\Omega}$. The former are defined by

$$\boldsymbol{J}_t^{\mathrm{E}}=\boldsymbol{I}_t^{\mathrm{E}}\delta(\boldsymbol{\rho}-\boldsymbol{\rho}'),\quad J_z^{\mathrm{M}}=I_z^{\mathrm{M}}\delta(\boldsymbol{\rho}-\boldsymbol{\rho}') \tag{9a}$$

for the TE case, and

$$J_z^{\mathrm{E}}=I_z^{\mathrm{E}}\delta(\boldsymbol{\rho}-\boldsymbol{\rho}'),\quad \boldsymbol{J}_t^{\mathrm{M}}=\boldsymbol{I}_t^{\mathrm{M}}\delta(\boldsymbol{\rho}-\boldsymbol{\rho}') \tag{9b}$$

for the TM case. Then, the fields at $\boldsymbol{\rho}$ due to these currents are given by

$$\boldsymbol{F}(\boldsymbol{\rho})=\mathbb{G}^{\Omega}(\boldsymbol{\rho},\boldsymbol{\rho}')\boldsymbol{I}, \tag{10}$$

where

$$\boldsymbol{F}=(F_z,\boldsymbol{F}_t)^T=\begin{cases}(H_z,\boldsymbol{E}_t)^T, & \text{TE},\\ (E_z,\boldsymbol{H}_t)^T, & \text{TM},\end{cases} \tag{11a}$$

likewise,

$$\boldsymbol{I}=(I_z,\boldsymbol{I}_t)^T=\begin{cases}\left(I_z^{\mathrm{M}},\boldsymbol{I}_t^{\mathrm{E}}\right)^T, & \text{TE},\\ \left(I_z^{\mathrm{E}},\boldsymbol{I}_t^{\mathrm{M}}\right)^T, & \text{TM},\end{cases} \tag{11b}$$

and where $\mathbb{G}^{\Omega}(\boldsymbol{\rho},\boldsymbol{\rho}')$ is given by

$$\mathbb{G}^{\Omega}=\begin{cases}\begin{pmatrix}i\omega\epsilon & \mathbb{L}'\\ -\mathbb{L} & \frac{i}{\omega\epsilon}\mathbb{L}\mathbb{L}'\end{pmatrix}G^{\Omega}(\boldsymbol{\rho},\boldsymbol{\rho}'), & \text{TE},\\ \begin{pmatrix}i\omega\mu & -\mathbb{L}'\\ \mathbb{L} & \frac{-i}{\omega\mu}\mathbb{L}\mathbb{L}'\end{pmatrix}G^{\Omega}(\boldsymbol{\rho},\boldsymbol{\rho}'), & \text{TM},\end{cases} \tag{11c}$$

with

$$\mathbb{L}=\nabla_t\times\hat{\boldsymbol{z}}-i\bar{\Omega}k_0^2\boldsymbol{\rho},\quad \mathbb{L}'=\nabla_t'\times\hat{\boldsymbol{z}}+i\bar{\Omega}k_0^2\boldsymbol{\rho}'. \tag{11d}$$

C. Boundary and continuity conditions for $\mathcal{R}^{\Omega}$ problem and numerical solutions

The boundary and continuity conditions (BCs) for the fields follow directly from ME. Since the rotation footprint appears only via the constitutive relations in Eqs. (1a) and (1b), it follows that the BCs for the tangential $\boldsymbol{E}$ and $\boldsymbol{H}$ in $\mathcal{R}^{\Omega}$ problem are precisely the same as those for the conventional $\mathcal{R}^0$ problem, thus they do not carry any effects of Ω. The normal components BCs may carry such an effect, as they satisfy (see Appendix B for details)

$$\hat{\boldsymbol{n}}\cdot(\epsilon_1\boldsymbol{E}_1-\epsilon_2\boldsymbol{E}_2)=\eta_{\mathrm{f}}-c^{-2}\Omega\rho\hat{\boldsymbol{\theta}}\cdot\boldsymbol{K}_{\mathrm{f}}, \tag{12a}$$

$$\hat{\boldsymbol{n}}\cdot(\mu_1\boldsymbol{H}_1-\mu_2\boldsymbol{H}_2)=0, \tag{12b}$$

where $\eta_{\mathrm{f}},\boldsymbol{K}_{\mathrm{f}}$ are the surface densities of the free electric charge and current. It is interesting to note that the rotation has no effect on the BCs for normal $\mu\boldsymbol{H}$ (not $\boldsymbol{B}$) for $\mathcal{R}^{\Omega}$ problem. Furthermore, the only presence of rotation in the BCs for normal $\epsilon\boldsymbol{E}$ is via the last term on the right of Eq. (12a). This term vanishes if the boundary cannot support free electric current. Therefore, if the structure consists of dielectric materials only, then it follows that the BCs for the complete $\boldsymbol{E}$ and $\boldsymbol{H}$ fields are the same as in conventional $\mathcal{R}^0$ problems. The practical importance of this observation cannot be overemphasized; it means that one may use conventional legacy numerical codes developed initially for $\mathcal{R}^0$ problems (such as the method of moments [26]), and apply them to solve $\mathcal{R}^{\Omega}$ problems merely by replacing the Green function with the one provided here in Eq. (5) or Eq. (7a). This approach is applied in the examples below.

D. Scattering and polarizability theory in $\mathcal{R}^{\Omega}$

The response of a scatterer to an incident field consists of electric and magnetic polarization currents only. These are given by $\boldsymbol{J}^{\mathrm{EP}}=-i\omega\boldsymbol{P}$ and $\boldsymbol{J}^{\mathrm{MP}}=-i\omega\mu_0\boldsymbol{M}$, where $\boldsymbol{P},\boldsymbol{M}$ are the electric and magnetic polarization densities, respectively. In conventional $\mathcal{R}^0$ problems they are related to $\boldsymbol{D},\boldsymbol{B}$ via $\boldsymbol{D}=\epsilon_0\boldsymbol{E}+\boldsymbol{P}$ and $\boldsymbol{B}=\mu_0(\boldsymbol{H}+\boldsymbol{M})$. In $\mathcal{R}^{\Omega}$ problems these relations do not hold since the $\boldsymbol{\Omega}$-dependent components in Eqs. (1a) and (1b) are in fact a result of space-time transformation of the fields and do not contribute directly to actual radiation. This fundamental property is derived and pointed out in Ref. [1] by using an electron-theoretic analysis in

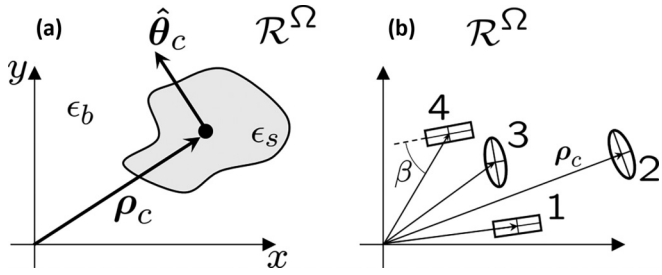

FIG. 2. (a) A single scatterer of homogeneous material ϵ_s and cross section area A of arbitrary shape, embedded in a background homogenous medium ϵ_b. The scatterer center of mass location $\boldsymbol{\rho}_c$ is arbitrary. The entire structure (scatterer and background) rotates rigidly around the origin at angular velocity $\boldsymbol{\Omega} = \hat{\boldsymbol{z}}\Omega$. We observe it at its rest FoR $\mathcal{R}^\Omega$. (b) Canonical examples of symmetries with respect to the rotation axis. The rotation footprint on $\sigma_{zz}^{\rm TM}$ ($\sigma_{z\rho}^{\rm TM}$) is always second (first) order in Ω. However, the footprint on $\sigma_{z\theta}^{\rm TM}$ is second order in Ω for scatterers possessing reflection symmetry across the line $\boldsymbol{\rho}_c$, scatterers #1,2, and first order in Ω for scatterers lacking this symmetry, e.g., scatterers#3,4 for $\beta \neq 0, \pi/2$ (see details in Appendix D).

noninertial FoR. The polarization densities that generate polarization currents are [1]

$$\boldsymbol{P} = \boldsymbol{D} - \epsilon_0 \boldsymbol{E} + c^{-2}(\boldsymbol{\Omega} \times \boldsymbol{r}) \times \boldsymbol{H}, \tag{13a}$$

$$\mu_0 \boldsymbol{M} = \boldsymbol{B} - \mu_0 \boldsymbol{H} - c^{-2}(\boldsymbol{\Omega} \times \boldsymbol{r}) \times \boldsymbol{E}, \tag{13b}$$

that together with Eqs. (1a) and (1b) yield $\boldsymbol{J}^{\rm EP} = -i\omega\epsilon_0\chi_e\boldsymbol{E}$ and $\boldsymbol{J}^{\rm MP} = -i\omega\mu_0\chi_m\boldsymbol{H}$, identical in form to the $\mathcal{R}^0$ polarization currents. The rotation footprint is manifested implicitly only, through the dependence of $\boldsymbol{E}, \boldsymbol{H}$ on Ω. Consider now a scatterer made of a material with χ_e^s, χ_m^s embedded in a homogeneous background with χ_e^b, χ_m^b. The polarization currents that radiate the *scattered* fields are given by

$$\boldsymbol{J}_{\rm rad}^{\rm EP} = -i\omega\epsilon_0\big(\chi_e^s - \chi_e^b\big)\boldsymbol{E}, \tag{14a}$$

$$\boldsymbol{J}_{\rm rad}^{\rm MP} - i\omega\mu_0\big(\chi_m^s - \chi_m^b\big)\boldsymbol{H}, \tag{14b}$$

where $\boldsymbol{E}, \boldsymbol{H}$ are the full EM fields in the presence of the scatterer. These polarization currents are spatially limited to the domain of the scatterer, and radiate in the background medium. A scattering problem can be effectively represented by Eqs. (2)–(4b) written for the background medium and with the currents above used to synthesize the sources $S^{\rm TE}$, $S^{\rm TM}$. As we show below, this is consistent with an independent and exact solution procedure of Eqs. (2)–(4a).

Consider the homogeneous scatterer shown schematically in Fig. 2, with cross-section area A and center of mass $\boldsymbol{\rho}_c$ defined via

$$\int_A (\boldsymbol{\rho} - \boldsymbol{\rho}_c) ds = \boldsymbol{0}. \tag{15}$$

If the scatterer is electrically small, then we can relate its spatially averaged internal fields $(\bar{F}_z, \bar{\boldsymbol{F}}_t) = (\bar{H}_z, \bar{\boldsymbol{E}}_t)$ [or $= (\bar{E}_z, \bar{\boldsymbol{H}}_t)$] for TE (or TM), to the incident fields at the scatterer center of mass $\boldsymbol{\rho}_c$, namely $F_z^i(\boldsymbol{\rho}_c), \boldsymbol{F}_t^i(\boldsymbol{\rho}_c)$. We express this relation via the internal scattering matrix $\boldsymbol{\sigma}(\Omega, \boldsymbol{\rho}_c)$

$$\begin{pmatrix} \bar{F}_z \\ \bar{\boldsymbol{F}}_t \end{pmatrix} = \begin{pmatrix} \sigma_{zz} & \boldsymbol{\sigma}_{zt} \\ \boldsymbol{\sigma}_{tz} & \boldsymbol{\sigma}_{tt} \end{pmatrix} \begin{pmatrix} F_z^i \\ \boldsymbol{F}_t^i \end{pmatrix}. \tag{16}$$

$\boldsymbol{\sigma}$ can be obtained either numerically by using conventional codes developed initially for solving $\mathcal{R}^0$ problems (see Sec. II C) or by approximate analytical methods; both are examined below. It depends not only on the scatterer "conventional" properties (e.g., geometry, material, etc...) but also on Ω and $\boldsymbol{\rho}_c$; the latter signifies its location with respect to the rotation axis. A word of caution is in order. The above formally holds if $\boldsymbol{\sigma}$ is written in a coordinate system that is not curved, at least locally. A cartesian system is appropriate. Since $\mathcal{R}^\Omega$ problems conform naturally with the cylindrical system it may be more convenient to use the latter, if the scatterer transverse dimensions (e.g., diameter) are much smaller than its distance from the rotation axis. Without loss of generality, assume it is located on the x axis. Then within the scatterer cross-section $\hat{\boldsymbol{x}} \simeq \hat{\boldsymbol{\rho}}$, $\hat{\boldsymbol{y}} \simeq \hat{\boldsymbol{\theta}}$. For an electrically small scatterer this assumption is reasonable, unless its center coincides with the rotation axis. In the latter case the rotation-induced effects are vanishingly small (see below). Under these assumptions, the scatterer polarizability matrix $\boldsymbol{\alpha}$ that relates the incident fields to the net currents is

$$\boldsymbol{\alpha} = -i\omega A \boldsymbol{\zeta} \boldsymbol{\sigma}, \tag{17a}$$

where A is the scatterer cross-section area, and with

$$\boldsymbol{\zeta} = \begin{cases} \mathrm{diag}(\mu_0 \Delta\chi_m, \epsilon_0 \Delta\chi_e \mathbf{I}_2), & \text{TE}, \\ \mathrm{diag}(\epsilon_0 \Delta\chi_e, \mu_0 \Delta\chi_m \mathbf{I}_2), & \text{TM}. \end{cases} \tag{17b}$$

Here $\mathbf{I}_2$ is the 2×2 identity matrix, and $\Delta\chi_{e,m} = \chi_{e,m}^s - \chi_{e,m}^b$.

Consider now the structure shown in Fig. 1. In consists of N scatterers, with center of mass locations $\boldsymbol{\rho}_n$ and polarizabilities $\boldsymbol{\alpha}_n$, $n = 1, \ldots N$. The latter may depend on Ω as well as on $\boldsymbol{\rho}_n$ due to the rotation, via the corresponding dependence of $\boldsymbol{\sigma}_n$. The structure response to an incident field $\boldsymbol{F}^i$ is governed by

$$\boldsymbol{I}_n = \boldsymbol{\alpha}_n \sum_{m \neq n}^{N} \mathbb{G}^\Omega(\boldsymbol{\rho}_n, \boldsymbol{\rho}_m) \boldsymbol{I}_m + \boldsymbol{\alpha}_n \boldsymbol{F}^i(\boldsymbol{\rho}_n), \quad n = 1, \ldots N, \tag{18}$$

where $\boldsymbol{I}_n$ are the polarization currents excited in the nth scatterer, defined in accordance to Eq. (11b). Below we study this formulation for dielectric structures.

III. TM EXCITATION

A. Electrically small scatterers

Since the structure is dielectric only, we have $\Delta\chi_m = 0$ and no magnetic polarization currents exist. Furthermore, we have

$$\boldsymbol{\alpha}^{\rm TM} = -i\omega A \epsilon_0 \Delta\chi_e \begin{pmatrix} \sigma_{zz}^{\rm TM} & \boldsymbol{\sigma}_{zt}^{\rm TM} \\ \mathbf{0} & \mathbf{0} \end{pmatrix}. \tag{19}$$

Then the formulation in Eq. (18) reduces to (spatially averaged internal fields are assumed, and the over-bar is ommitted

for convenience)

$$I^{\mathrm{EP}}_{z\,n} = -i\omega C_n \sum_{m\neq n}^{N} \left(i\omega\mu\sigma^{\mathrm{TM}}_{zz\,n} + \boldsymbol{\sigma}^{\mathrm{TM}}_{zt\,n}\cdot\mathbb{L}\right) G^{\Omega}(\boldsymbol{\rho}_n, \boldsymbol{\rho}_m) I^{\mathrm{EP}}_{z\,m}$$
$$-i\omega C_n\left[\sigma^{\mathrm{TM}}_{zz\,n} E^i_z(\boldsymbol{\rho}_n) + \boldsymbol{\sigma}^{\mathrm{TM}}_{zt\,n}\cdot\boldsymbol{H}^i_t(\boldsymbol{\rho}_n)\right], \tag{20a}$$

where

$$C_n = A_n\epsilon_0(\Delta\chi_e)_n. \tag{20b}$$

The term $\mathbb{L}G^{\Omega}(\boldsymbol{\rho}_n, \boldsymbol{\rho}_m)$ in Eq. (20a) is in fact the transverse magnetic field $\boldsymbol{H}_t$ at $\boldsymbol{\rho} = \boldsymbol{\rho}_n$ due to a $\hat{z}$-directed unit electric current at $\boldsymbol{\rho}' = \boldsymbol{\rho}_m$. It is given explicitly in Appendix C. $\sigma^{\mathrm{TM}}_{zz\,n}$ and $\boldsymbol{\sigma}^{\mathrm{TM}}_{zt\,n}$ are the $\boldsymbol{\sigma}$ matrix components that correspond to the nth scatterer, constituting the crucial part of the polarizability operator $\boldsymbol{\alpha}$. It is interesting to note that $\boldsymbol{\sigma}_{zt}$ represents the coupling between the incident $\boldsymbol{H}_t$ and the scatterer's internal E_z. In $\mathcal{R}^0$ problems this element vanishes if the scatterer is electrically small and nonmagnetic (i.e., if $\Delta\chi_m = 0$). However, as we show below in $\mathcal{R}^{\Omega}$ problems it is formally non zero—albeit perhaps small—due to the inherent rotation-induced electric-magnetic coupling. This coupling has been observed even for *static* fields in $\mathcal{R}^{\Omega}$ problems [7]. Below we turn to study the scattering matrix $\boldsymbol{\sigma}$ (and consequently, the polarizability $\boldsymbol{\alpha}$) and its components for an individual scatterer.

We assume that the scatterer of arbitrary cross section area $A(\boldsymbol{\rho}_c)$ is made of a uniform dielectric material with susceptibility $\chi^s_e = \epsilon^s_r - 1$, embedded in a homogeneous medium with $\chi^b_e = \epsilon^b_r - 1$, and with center of mass $\boldsymbol{\rho}_c$. From Eq. (2) E_z satisfies the integral equation

$$E_z(\boldsymbol{\rho}) = E^i_z(\boldsymbol{\rho}) + k_0^2 C\int_{A(\rho_c)} G^{\Omega}(\boldsymbol{\rho}, \boldsymbol{\rho}')E_z(\boldsymbol{\rho}')ds', \tag{21}$$

where $C = n^2 - n_b^2 = \mu_r\Delta\chi_e$ is the scatterer contrast, and $G^{\Omega}(\boldsymbol{\rho}, \boldsymbol{\rho}')$ is the background medium Greens function, i.e., it is given by Eqs. (7a) and (7b) with the refraction index $n = n_b = \sqrt{\mu_r\epsilon^b_r}$. Note that the role of $\boldsymbol{\rho}_c$ in the area A is significant since $G^{\Omega}(\boldsymbol{\rho}, \boldsymbol{\rho}')$ is not shift-invariant. This exact integral equation, that follows rigorously from Eq. (2), shows that the radiating current that generates the scattered field is indeed given by Eq. (14a).

Since the scatterer is electrically small, any electric field quantity (whether incident or total) E_z is approximately uniform within $A(\boldsymbol{\rho}_c)$. The local spatial variations of E_z within the scatterer cross section can be expressed effectively via the corresponding local $\boldsymbol{H}_t$. To correctly capture the rotation footprint on both $E_z, \boldsymbol{H}_t$ and hence on $\sigma^{\mathrm{TM}}_{zz}$ and $\boldsymbol{\sigma}^{\mathrm{TM}}_{zt}$, we endeavor to establish an $\bar{\Omega}$-induced point-wise connection between $E_z(\boldsymbol{\rho})$ and $E^i_z(\boldsymbol{\rho}_c), \boldsymbol{H}^i_t(\boldsymbol{\rho}_c)$. This relation is derived in Appendix D, resulting in the explicit expressions for the scattering matrix in Eqs. (D4a)–(D4c). We also study the dominant behavior of $\sigma^{\mathrm{TM}}_{zz}$ and $\boldsymbol{\sigma}^{\mathrm{TM}}_{zt}$ in terms of a power series in Ω. Its importance is twofold. It indicates which entry of $\boldsymbol{\sigma}^{\mathrm{TM}}$ may potentially be important in the limit of slow rotation (e.g., second-order terms are negligible). Furthermore, Ω^2 is insensitive to rotation direction, while Ω dependence changes sign when direction is reversed, meaning it senses direction; the power-series study reveals novel physical properties.

Examples based on exact computations of Eqs. (D4a)–(D4c) are shown in Fig. 3. The results are consistent with

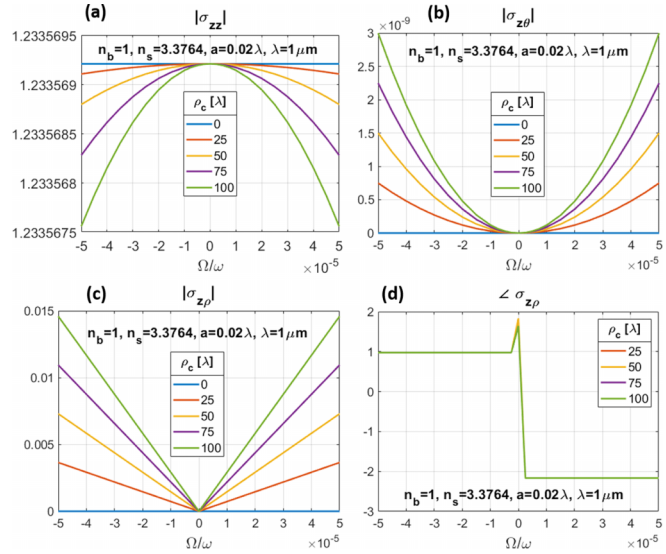

FIG. 3. Entries of the scattering matrix $\boldsymbol{\sigma}^{\mathrm{TM}}$ vs $\bar{\Omega}$, for dielectric cylindrical scatterers with radius $a = 0.02$ μm and $\epsilon_s = 11.4$ in a vacuum background and for $\lambda = 1$ μm. ρ_c is the distance of the scatterer center from the rotation axis. The results were obtained using the explicit analytic expressions in Eqs. (D4a)–(D4c). (a) $|\sigma^{\mathrm{TM}}_{zz}|$. For $\Omega = 0$ it reduces to the scattering matrix value of the corresponding $\mathcal{R}^0$ problem. The rotation footprint is second order in Ω and its effect on $\sigma^{\mathrm{TM}}_{zz}$ is $\mathcal{O}(10^{-7})$ relative to its $\mathcal{R}^0$ value. (b) $|\sigma^{\mathrm{TM}}_{z\theta}|$. (c) $|\sigma^{\mathrm{TM}}_{z\rho}|$. (d) The phase of $\sigma^{\mathrm{TM}}_{z\rho}$ in radians.

the general predictions derived in Appendix D. As seen from the analysis and the figures, the rotation footprint on $\sigma^{\mathrm{TM}}_{zz}$ and on $\sigma^{\mathrm{TM}}_{z\theta}$ is second order in $\Omega\rho_c$ for circular cylinders, thus negligible in the limit of slow rotation. We note that this second-order dependence holds also for the phase of $\sigma^{\mathrm{TM}}_{zz}$ (not shown). The rotation footprint on $\sigma^{\mathrm{TM}}_{z\rho}$ is linear with $\bar{\Omega}$, thus representing a new rotation-induced physical effect. Furthermore, it affects the magnitude only, while the phase of $\sigma^{\mathrm{TM}}_{z\rho}$ is independent of Ω or ρ_c. The π phase jump across $\bar{\Omega} = 0$ indicates that this response is indeed essentially a straight line passing through the origin, and thus it is sensitive to the rotation direction. However, up to $\bar{\Omega} = 5\times10^{-5}$ with $\lambda = 1$ μm, the corresponding rotation rate is about 15 GHz, far beyond realistic frequencies for a PA structure. For $\rho_c = 100\lambda$, that correspond to linear speed of $\mathcal{O}(0.03c)$, this footprint is $\mathcal{O}(10^{-2})$. A realistic comparison to $|\sigma^{\mathrm{TM}}_{zz}|$ should be done with the normalized value $\eta^{-1}|\sigma^{\mathrm{TM}}_{z\rho}|$ so both elements have the same physical units. For realistic rotation rates the effects of the latter is well below 10^{-5} compare to the former. Thus, although novel, it is generally too weak to have a significant impact on a PA response.

The above observations do not necessarily mean that the rotation does not have a significant effect on a rotating structure that consists of a large number of electrically small inclusions. We show below that the effect of rotation is manifested essentially via the propagation of the multiply scattered fields inside the structure.

Figure 4 shows the same as Fig. 3, for a dielectric scatterer of rectangular shape with dimensions of 42×8.4 nm^2 and the same material and wavelength, but for two different

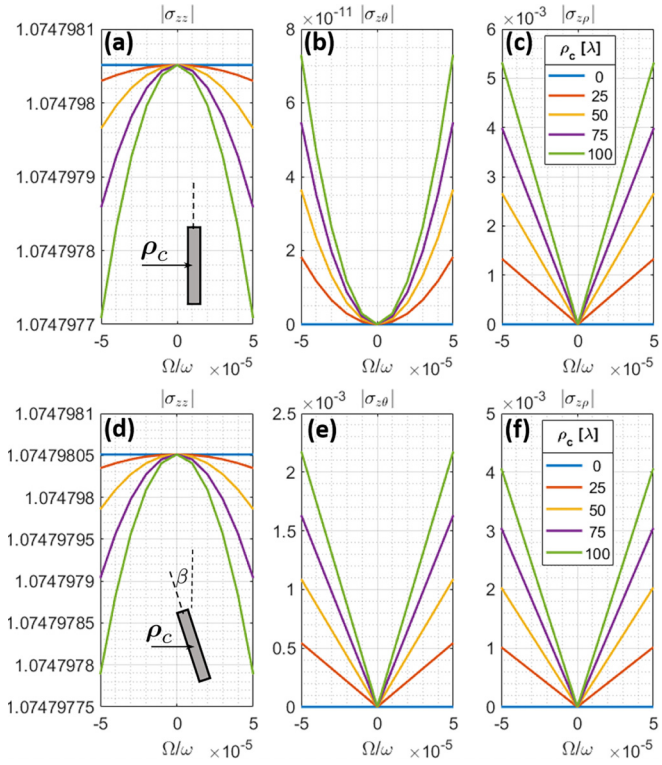

FIG. 4. Entries of the scattering matrix $\boldsymbol{\sigma}^{\mathrm{TM}}$ vs $\bar{\Omega}$, for a dielectric scatterer of rectangular shape with dimensions of 42×8.4 nm and $\epsilon_s = 11.4$ in a vacuum background and for $\lambda = 1$ μm. ρ_c is the distance of the scatterer center from the rotation axis. The results were obtained using the explicit analytic expressions in Eqs. (D4a)–(D4c). (a–c) $|\sigma_{zz}^{\mathrm{TM}}|$, $|\sigma_{z\theta}^{\mathrm{TM}}|$ and $|\sigma_{z\rho}^{\mathrm{TM}}|$, when the larger dimension is normal to $\boldsymbol{\rho}_c$. (d–f) The same as panels (a–c) but with inclination angle $\beta = \pi/6$. Breach of symmetry with respect to $\boldsymbol{\rho}_c$ results in first-order dependence of $\sigma_{z\theta}$ on Ω.

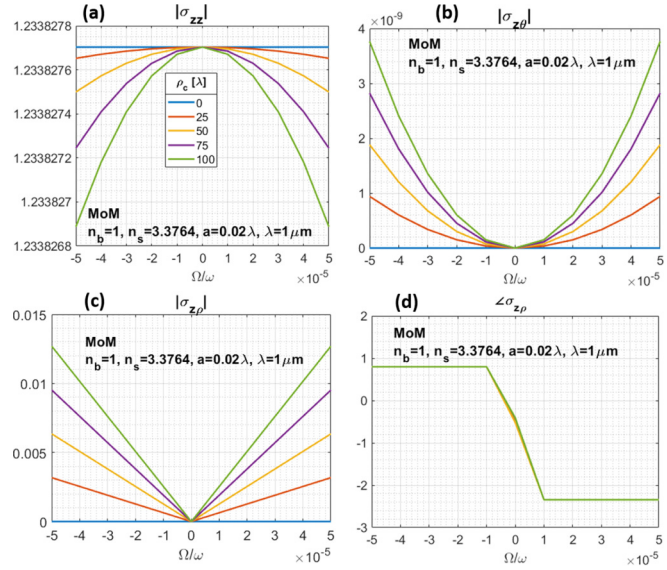

FIG. 5. The same as described in the caption of Fig. 4, but as obtained by the volumetric method of moments numerical approach in conjunction with the procedure described in Appendix E.

inclinations with respect to $\boldsymbol{\rho}_c$. It is seen that breach of symmetry with respect to the latter indeed changes fundamentally the dependence of $\sigma_{z\theta}$ on Ω—it becomes first order in Ω. However, the rotation footprint on the scattering parameters is still too small to be significant in realistic rotation rates of PAs.

We turn to demonstrate the main features of $\boldsymbol{\sigma}^{\mathrm{TM}}(\bar{\Omega}, \boldsymbol{\rho}_c)$ by using a purely numerical approach. As pointed out in Sec. II C, legacy codes can be adapted to solve $\mathcal{R}^{\Omega}$ problems merely by replacing the Green function routine. Here we use the volumetric method of moments (MoM) to obtain numerical solutions of integral equations of the type presented in Eq. (21)—see Ref. [26] for details of this approach. From the set of numerical solutions to different excitations one may extract the scattering matrix entries. Since the rotation footprint numerical values are widely separated, spanning a large range of orders, we exercise special care to stabilize the computation by applying suitable preprocessing and post-processing procedures. Details are provided in Appendix E. Figure 5 shows the results for the same scatterer of Fig. 3. There is a mutual consistency with respect to the general properties of the rotation footprint and numerical agreement within the range of 10–25%.

B. Particle array dynamics

The electrodynamics of an array consisting of a large number of electrically small 2D scatterers can now be studied using the formulation in Eqs. (18)–(20b), with $\boldsymbol{\sigma}^{\mathrm{TM}}(\Omega, \boldsymbol{\rho}_c)$ and $\boldsymbol{\alpha}(\Omega, \boldsymbol{\rho}_c)$ discussed in Sec. III A. Although their dependence on Ω and $\boldsymbol{\rho}_c$ can be somewhat simplified by the power-series approach discussed there, it may pose a significant practical challenge when dealing with structures consisting of a large number of inclusions and attempting to compute $\boldsymbol{\alpha}(\Omega, \boldsymbol{\rho}_c)$ individually for each one. This difficulty may be alleviated if the contribution of $\boldsymbol{\alpha}(\Omega, \boldsymbol{\rho}_c)$ to the rotation footprint on the PA response is subdominant compare to that due to the inter-particle propagations as manifested by G^{Ω}. Then $\boldsymbol{\alpha}(\Omega, \boldsymbol{\rho}_c)$ can be replaced by its value in the corresponding $\mathcal{R}^0$ problem, namely $\boldsymbol{\alpha}(0, \mathbf{0})$, without significant effect on the rotation-induced dynamics. Then the formulation in Eqs. (18)–(20b) reduces to

$$I_n = i\omega\mu\alpha_n \sum_{m\neq n}^{N} I_m G^{\Omega}(\boldsymbol{\rho}_n, \boldsymbol{\rho}_m) + \alpha_n E_z^i(\boldsymbol{\rho}_n),$$
$$n = 1, \ldots N, \tag{22}$$

where α_n is the scalar polarizability of the nth inclusion in the $\mathcal{R}^0$ problem. In the above formulation rotation is manifested only via G^{Ω}. We tested the simplified formulation in Eq. (22) and compared it to exact numerical simulations using two *independent* numerical methods. The first is the aforementioned volumetric MoM used in the previous subsection. The second is the multifilaments methods [27]—a special variant of the method of moment. As mentioned in Sec. II C, legacy codes can be adapted to solve $\mathcal{R}^{\Omega}$ problems merely by replacing the Green function routine—as has already been applied successfully in Ref. [15] to study rotating photonic crystals. The array is shown in Fig. 6(a). The total number of scatterers is

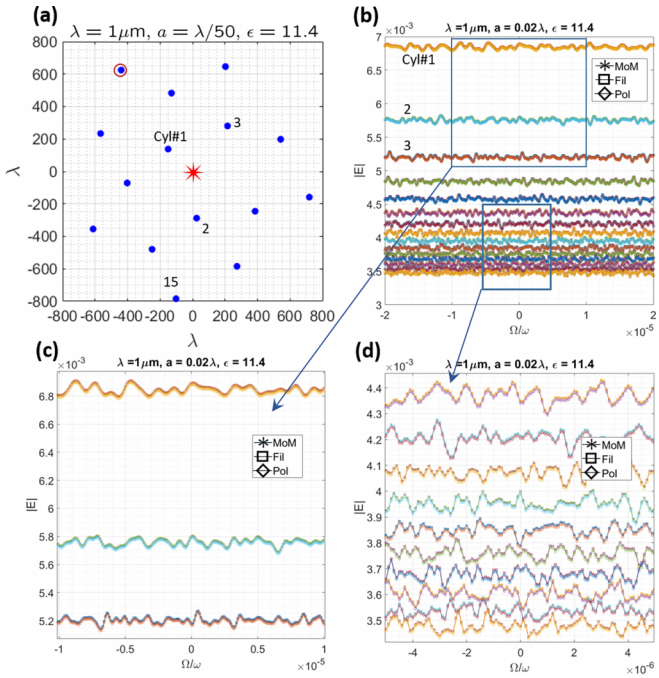

FIG. 6. Rotating array response in $\mathcal{R}^{\Omega}$. (a) The array geometry. The cylinders properties are the same as those of Fig. 3. The red circle shows the cylinder with the highest sensitivity to rotation in the limit of $\Omega \to 0$. (b) The electric field in the cylinders centers, using three different and independent computations; the volumetric method of moments (MoM), the method of filaments (Fil), and the polarizability theory approach in Eq. (22) (Pol) where α is the $\mathcal{R}^0$ problem polarizability (i.e., α of nonrotating scatterers). (c, d) Zoom into the indicated regions.

relatively small to keep the full-wave numerical solutions within reasonable computation times. Thus, we have $N = 15$ dielectric cylinders with the same parameters as those of Fig. 3. To concentrate our attention on the rotation-induced effects only, we minimize any long-range order effects by choosing an array that is not periodic nor quasiperiodic. The golden angle spiral is such an array that was previously studied in photonic crystal applications [28]. The nth particle location is given by the cylindrical coordinates $(\rho_n, \phi_n) = (a_0\sqrt{n}, n\phi)$, where $\phi = 8\pi/(1+\sqrt{5})^2$ is the Golden Angle. a_0 is an arbitrary reference distance here chosen to be $a_0 = 200\lambda$. The structure is excited by a $\hat{z}$-directed electric line source at the origin, with $\lambda = 1$ μm. Figures 6(b)–6(d) show the absolute value of the electric field excited at the center of each cylinder, as a function of the normalized rotation rate $\bar{\Omega} = \Omega/\omega$, obtained by using three independent methods; the two independent numerical methods and the reduced formulation of polarizability theory (Pol) in Eq. (22). Excellent agreement between the methods is evident, over the extremely large range of rotation rates. This internal electric field is related to the cylinders polarization current densities via Eq. (14a). It is of interest to zoom into the range of extremely small rotation rates. Figure 7 shows $|I_n(\Omega)|$ normalized to their respective values at $\Omega = 0$ (or the electric fields). Generally, the response is a complex and nonsymmetric function of Ω, but as $\Omega \to 0$ it becomes linear. This behavior suggests to define the array sensitivity to rotation as

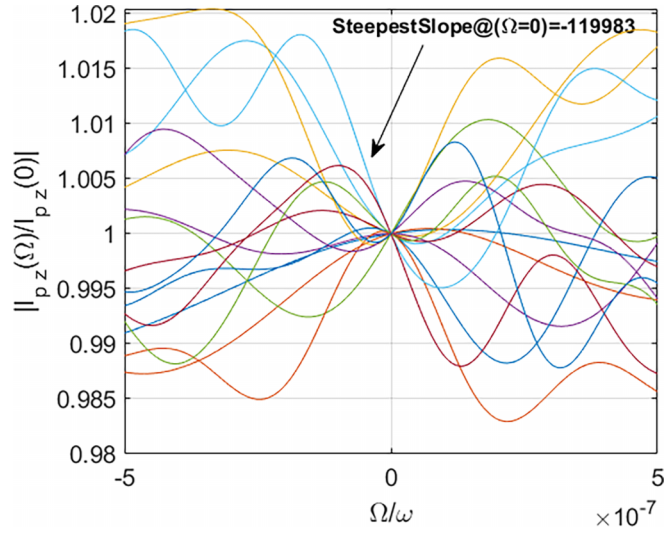

FIG. 7. Rotating array response in $\mathcal{R}^{\Omega}$ normalized to their values at $\Omega = 0$. Note the linear behavior at the origin. The cylinder with the largest slope satisfies Eq. (23). It is marked by a red circle in Fig. 6.

the *maximal slope* at $\Omega = 0$,

$$S = \max_{n=1,\ldots N} \lim_{\Omega \to 0} \frac{1}{\bar{\Omega}} \left| \frac{I_n(\Omega)}{I_n(0)} - 1 \right|, \tag{23}$$

where, to avoid extreme values due to division by vanishing currents, we exclude all cylinders with $|I_n|$ smaller than 1% of the average current in the array. This sensitivity figure may form a basis for a new class of metamaterial based rotation sensors, as explored in Ref. [29].

Since the solution of Eq. (22) with α_n of the corresponding $\mathcal{R}^0$ problem agrees so well with the full wave exact numerical solutions, we conclude that the reduced formulation in Eq. (22) carries the essential physics of particle arrays ED in $\mathcal{R}^{\Omega}$ problems for any practical rotation rate and for electrically small inclusions. This formulation can be used to study analytically the effect of rotation axis shift. Consider the system shown in Fig. 8. An array with scatterers locations $\boldsymbol{\rho}_n$ is excited by a line current source I_s at $\boldsymbol{\rho}'$. Thus, it is governed by

$$a_n I_n - \sum_{m \neq n}^{N} G^{\Omega}(\boldsymbol{\rho}_n, \boldsymbol{\rho}_m) I_m = G^{\Omega}(\boldsymbol{\rho}_n, \boldsymbol{\rho}') I_s, \tag{24a}$$

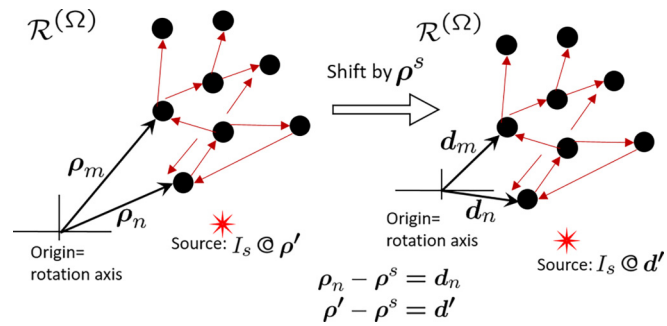

FIG. 8. Shift by $\boldsymbol{\rho}^s$ of the entire array and the exciting source.

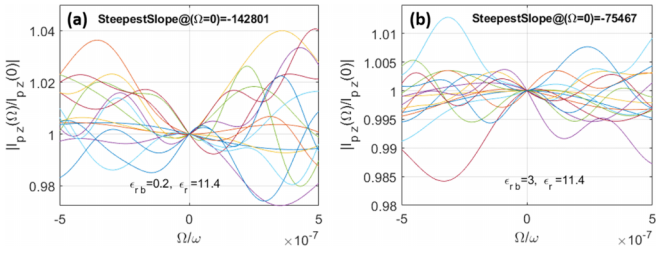

FIG. 9. The normalized currents for different background index (a) $\epsilon_{rb} = 0.2$. (b) $\epsilon_{rb} = 3$.

where $a_n = (i\omega\mu\alpha_n)^{-1}$. If the structure and the source are shifted by $\boldsymbol{\rho}^s$, then the new currents I_n^s are governed by

$$a_n I_n^s - \sum_{m\neq n}^{N} G^{\Omega}(\boldsymbol{d}_n, \boldsymbol{d}_m) I_m^s = G^{\Omega}(\boldsymbol{d}_n, \boldsymbol{d}') I_s, \tag{24b}$$

where $\boldsymbol{d}_n = \boldsymbol{\rho}_n - \boldsymbol{\rho}^s$ and $\boldsymbol{d}' = \boldsymbol{\rho}' - \boldsymbol{\rho}^s$. Using now Eq. (8b) it is straightforward to show that I_n and I_n^s are related by the *diagonal transformation*

$$I_n^s = I_n e^{ik_0^2 \bar{\Omega}\hat{z}\cdot[\boldsymbol{\rho}^s \times (\boldsymbol{d}' - \boldsymbol{d}_n)]}, \quad \forall n, \tag{24c}$$

that is *phase-only*. Hence, the currents magnitude is invariant with respect to the rotation axis; $|I_n| = |I_n^s| \, \forall n$. This was verified by numerical simulations. Figures 6(b)–6(d) that show $|I_n|$ is invariant with respect to the location axis. The transformation in Eq. (24c) reveals an appealing property; a metamaterial based rotation sensor can be used not only to extract the rotation rate and its direction as seen from Fig. 7 and Eq. (23) [29], but once Ω is determined one may use Eq. (24c) to extract the distance from the rotation axis by measuring the currents relative phases.

It is interesting to contrast the result in Eq. (24c) with the phase of the response of a single inclusion—see Fig. 3 and the pertaining discussion in Sec. III A. While the latter is second order in $\Omega\rho_c$, the former is linear with $\Omega\rho_0$.

The transformation in Eq. (25c) carries on also to the scattered field $E_z(\boldsymbol{\rho})$ at *any* observation point $\boldsymbol{\rho}$. These fields, in the original and in the shifted system are given, respectively, by

$$E_z(\boldsymbol{\rho}) = i\omega\mu \sum_n I_n G^{\Omega}(\boldsymbol{\rho}, \boldsymbol{\rho}_n), \tag{25a}$$

$$E_z^s(\boldsymbol{\rho} - \boldsymbol{\rho}^s) = i\omega\mu \sum_n I_n^s G^{\Omega}(\boldsymbol{\rho} - \boldsymbol{\rho}^s, \boldsymbol{d}_n). \tag{25b}$$

Using Eqs. (24c) and (8b) in Eq. (25b) leads to

$$E_z^s(\boldsymbol{\rho} - \boldsymbol{\rho}^s) = E_z(\boldsymbol{\rho}) e^{ik_0^2 \bar{\Omega}\hat{z}\cdot[\boldsymbol{\rho}^s \times (\boldsymbol{\rho}' - \boldsymbol{\rho})]}, \quad \forall \boldsymbol{\rho}. \tag{25c}$$

It is also interesting to note that this relative phase is independent of the background material index n_b. The background material, however, does affect the PA sensitivity to rotation. Figure 9 shows the normalized response currents for low index background (a) and for high index background. The slopes and hence the sensitivity S in Eq. (23) decrease (increase) when the background refraction index increases (decreases).

To conclude the above observations note the following interesting points.

(1) The rotation footprint is almost exclusively dominated by the propagations taking place between the multiple scattering phenomena, presented rigorously by G^{Ω}. It has been shown that G^{Ω} is consistent with the Sagnac effect [25], and reconstructs the celebrated Sagnac phase shift ϕ_s within any closed loop of scattering events. Furthermore, ϕ_s is independent of the rotation axis location, and of the medium properties. This is consistent with the observations made in Eqs. (24a)–(24c).

(2) The system *sensitivity* depends on the background refraction index. This is in contrast to the classical Saganac shift ϕ_s. However, it is also known that the rotation-induced shifts of the resonance frequencies of rotating closed loops do depend on their refraction index, as seen in conventional ring-laser gyroscopes (RLG's) [30]. It is the result of the infinite multiplicity of interferences of the waves resonating in the structure. Thus, one may conclude that the internal ED of rotating particle arrays is dominated by the multiplicities of Sagnac loops created within the structure and their mutual interferences on two levels: first, between a large number of different loops (that are met on each scatterer), and second, on the self-interference and resonances of a loop that is repeating itself within the structure. This picture is further explored in Ref. [29].

(3) The system response is a highly nonsymmetric and nonmonotonic function of Ω. In the limit of slow rotation, however, the response of each scatterer is linear with Ω and it can be used to determine the sign of Ω and its value. Unlike the conventional Sagnac effect, however, here the information of the rotation axis location can also be extracted.

C. Resonances and collective effects

In the previous sections we dealt with electrically small scatterers that are far from their internal resonances, and with arrays that do not possess any strong collective resonance effects within the range of parameters shown. Here we turn to study the effect of rotation on the resonance of the single-inclusion scattering matrix, e.g., $\sigma_{zz}^{\mathrm{TM}}$, and on the collective effect of stop-band in a finite-size photonic crystal (PhC) structure.

The cylinders with moderate dielectric contrast studied in previous sections possess wave resonances at higher frequency and/or contrasts. To explore the rotation-induced effect on such resonances we have used the formulation developed in Appendix D for cylinders of the same radius of $a = 0.02$ μm but with $\epsilon_{rs} = 20$. The results are shown in Fig. 10. Figure 10(a) shows $\sigma_{zz}^{\mathrm{TM}}$ versus $k_0 a$ for the corresponding $\mathcal{R}^0$ problem (no rotation, laboratory frame). The resonance frequency is rigorously defined as the frequency at which $\Re\{\sigma_{zz}^{\mathrm{TM}}\} = 0$. Figure 10(b) shows the resonance frequency in terms of $k_0 a$ versus $\Omega/\omega*$ for various values of ρ_c, where $\omega*$ is the frequency corresponding to $\lambda = 0.5$ μm. It is seen that the rotation-induced shift of resonance is second order in both Ω and ρ_c. This dependence is in fact a direct result of the second-order dependence of the function ψ and the pertaining analysis in Appendix D and Eqs. (D3)–(D7). Furthermore, within the range of parameters tested here, the shift is considerably smaller than the natural line width of the resonance itself seen in Fig. 10(a). Thus, the effect of rotation on the microscopic

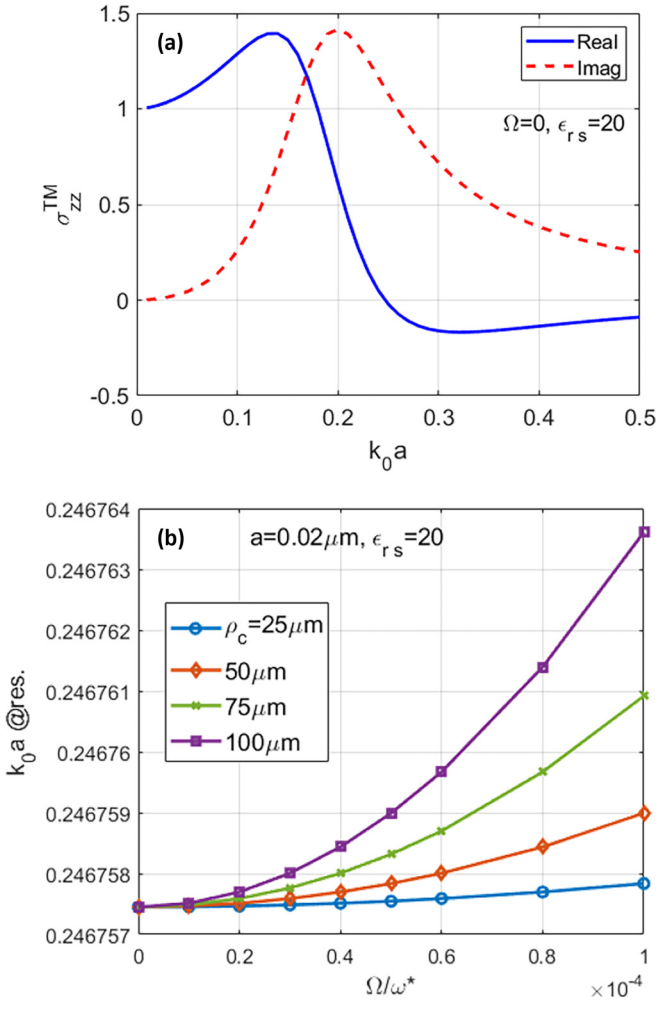

FIG. 10. The effect of rotation on the resonance of a single cylindrical scatterer with $\epsilon_{rs} = 20$. (a) $\sigma_{zz}^{\mathrm{TM}}$ without rotation. The resonance occurs at $\Re\{\sigma_{zz}^{\mathrm{TM}}\} = 0$. (b) Shift of the resonance frequency vs rotation rate for several values of ρ_c. ω^* is the optical frequency corresponding to $\lambda = 0.5$ μm.

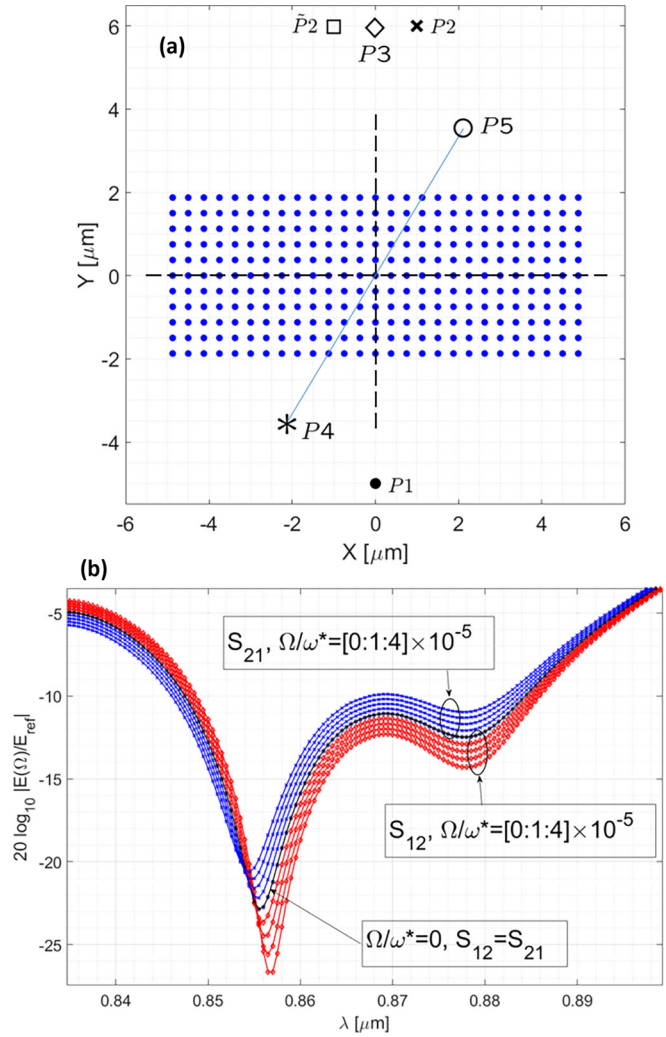

FIG. 11. The effect of rotation on the collective properties of a finite photonic crystal. (a) The PhC structure and the interchanging source/observation points. The PhC possesses mirroring symmetry over the dashed lines. $\tilde{P}2$ is the mirroring of $P2$ over the y axis. (b) S_{12} and S_{21} vs the optical wavelength for several values of Ω/ω^* where ω^* corresponds to $\lambda = 1$ μm. When $\Omega \mapsto -\Omega$ the curves S_{12} and S_{21} interchange. The same happens when $P2$ is replaced by its mirror image $\tilde{P}2$. $|S_{ij}|$ are independent of the rotation axis location.

wavelike resonances is relatively weak. The case of quasistatic LC-like resonance under rotation is studied in Ref. [7].

The effect of rotation on the collective properties of a periodic particle array is studied next. Due to the specific $\boldsymbol{r}$-dependent constitutive relations in Eqs. (1a)–(1b) the conventional Floquet-Bloch theorem and the ensuing band theory formally do not hold and cannot be used to solve our wave equation (2) even if $\epsilon(\boldsymbol{r})$, $\mu(\boldsymbol{r})$ are perfectly periodic. However, for finite-size PhC structure the stop-band still survives and can be observed in $\mathcal{R}^{\Omega}$ problems. Furthermore, the inherent nonreciprocity of $\mathcal{R}^{\Omega}$ affects the band-gap in a unique way.

We used the formulation in Eq. (22) to explore the rotation-induced effects on the band-gap of the finite PhC shown in Fig. 11(a). It consists of $27 \times 11 (x \times y)$ dielectric cylinders of radius $a = 0.1$ μm and $\epsilon_{rs} = 11.4$, arranged on a square lattice with period of 0.375 μm. The structure center is at the origin, coinciding with the rotation axis. The external points $P1 = (x_1, y_1) = (0, -5)$ μm and $P2 = (x_2, y_2) = (1, 6)$ μm are used interchangeably for source and observation locations. The reason for the asymmetric placement of $P2$ becomes clear below. We define $S_{ij}(\Omega)$ as the field measured at Pi due to a point source at Pj in the presence of the PhC—the $\mathcal{R}^{\Omega}$ problem, normalized to the reference field E_{ref} that is the same quantity but in the absence of the PhC and with no rotation at all ($\mathcal{R}^0$ problem, no PhC). Figure 11(b) shows $20 \log_{10} |S_{12}|$ and $20 \log_{10} |S_{21}|$, for Ω/ω^* ranging between 0 and 4×10^{-5}. Here ω^* is the frequency corresponding to $\lambda = 1$ μm. At $\Omega = 0$ the lines of S_{12} and S_{21} coincide due to reciprocity. For $\Omega > 0$, S_{12} red-shifts (slides rightward, shown in red) and S_{21} blue-shifts (slides leftward, shown in blue), at a rate that is linear in Ω. In addition, the deepest point in S_{12} (S_{21}) becomes deeper (shallower) as Ω increases. At the deepest point of S_{12} there is nearly an order of magnitude difference between S_{12} and S_{21} for the largest Ω shown. The magnitudes of S_{ij} are independent of the rotation axis, as

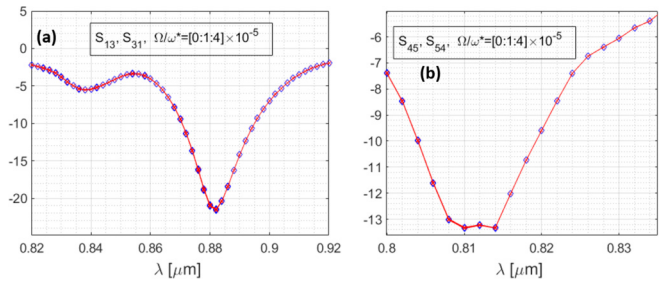

FIG. 12. The same as Fig. 11(b) for identical range of rotation rates, but different source and observation points. (a) S_{13} and S_{31} for the points $P1 = (0, -5)$ μm, $P3 = (0, 6)$ μm shown in Fig. 11(a); both points reside on the same PhC mirroring symmetry line. Consequently, the transmission is symmetrical and is not affected by rotation. (b) S_{45} and S_{54} for the points $P4 = (-2, -3.5)$ μm, $P5 = M_{\pi/2}M_0P4 = (2, 3.5)$ μm shown in Fig. 11(a). Again, the transmission is symmetrical and is not affected by rotation.

predicted by Eq. (25c) and tested numerically for the same structure but with a rotation axis shifted 500 μm leftward.

1. Symmetries

Several general symmetries of the rotation-induced PhC dynamics can be deduced directly from Eqs. (8a)–(8c) and Eqs. (24a)–(25c), in conjunction with the matrix form of Eq. (22) whose entries are nothing but $G^{\Omega}(\boldsymbol{\rho}_n, \boldsymbol{\rho}_m)$. These are

(1) Due to the inversion property in Eq. (8a), upon reversing the rotation direction $\Omega \mapsto -\Omega$ the lines of S_{12} and S_{21} precisely interchange.

(2) The PhC structure discussed above is symmetric under mirroring over the y axis. Then for any pair of the PhC points Eq. (8c) holds with $M_\theta = M_{\pi/2}$. Define $E^{\Omega}(Pi, Pj)$ as the field at Pi due to a source at Pj, for rotation rate Ω. Then

$$E^{\Omega}(Pi, Pj) = E^{-\Omega}(\tilde{P}i, \tilde{P}j). \tag{26a}$$

In the example in Fig. 11(a) $P1$ resides on a mirroring symmetry line, so $\tilde{P}1 = P1$. Thus, by replacing $P2$ by its $M_{\pi/2}$ mirror image $\tilde{P}2$, the transmissions S_{12} and S_{21} precisely interchange.

(3) If $P2$ is shifted to the y axis, then $P2$ and $\tilde{P}2$ coalesce to a single point P on the axis. It follows then that

$$E^{\Omega}(P1, P) = E^{-\Omega}(P1, P) = E^{-\Omega}(P, P1), \tag{26b}$$

whose only admissible solution, up to first order, is $E^{\Omega}(P1, P) = E^{0}(P1, P)\ \forall\,\Omega$. Thus, if both source and observer reside on the line of the PhC mirror symmetry, then Ω has no effect on the transmission properties and the asymmetry disappears. An example is shown in Fig. 12(a).

(4) Equation (8c) holds for multiple mirroring over different lines. Any even number of operations leaves the rotation footprint in G^{Ω} unchanged. We generally have

$$M_{\theta_1}M_{\theta_2} = R_{2(\theta_1-\theta_2)}, \tag{27}$$

where R_θ is a rotation by θ. Of particular interest are the two consecutive mirroring about the two lines of symmetry of the PhC; the y and x axes that correspond to $M_{\pi/2}$ and M_0, respectively. $M_{\pi/2}M_0$ yields an inversion through the center, that amounts to rotation by π. Let $P3$ and $P4$ two points satisfying $P3 = M_{\pi/2}M_0P4$. Then, from Eq. (8a), Eq. (8c), and the fact that our PhC structure is invariant under $M_{\pi/2}M_0$, we have

$$\begin{aligned} E^{\Omega}(P3, P4) &= E^{\Omega}(M_{\pi/2}M_0P3, M_{\pi/2}M_0P4) \\ &= E^{-\Omega}(P4, P3), \quad \forall\,\Omega, \end{aligned} \tag{28}$$

whose only admissible solution up to first order is $E^{\Omega}(P4, P3) = E^{\Omega}(P3, P4) = E^{0}(P3, P4)\ \forall\,\Omega$. Thus, if both source and observer are precisely interchangeable under an even number of mirroring operations over mirror-symmetry lines, then Ω has no effect on the transmission properties and the asymmetry disappears. An example is shown in Fig. 12(b).

IV. TE EXCITATION

Symmetry between TE and TM polarization exists only under the interchange $\epsilon \leftrightarrow \mu$. If the structure remains dielectric, then such symmetry cannot be exploited. Unfortunately, for dielectric structures Eq. (2) cannot be converted to a pure integral equation of the form of Eq. (21), but to an integrodifferential equation. Then, the scattering matrix $\boldsymbol{\sigma}$ (and hence the polarizability matrix $\boldsymbol{\alpha}$) cannot be studied by invoking the same tools; it will be addressed in a separate study. However, the results for TM polarization suggests that also in the TE case one may use the $\mathcal{R}^0$ problem polarizability and still convey the fundamental physics associated with the rotation of the *entire* MM structure, and with practically no sacrifice of accuracy.

From Eqs. (14a) and (14b) it follows that the radiating current is still due to the electric polarization. However, as in the $\mathcal{R}^0$ case, this current is a vector in the (x, y) plane thus $\boldsymbol{\alpha}$ is a 2×2 matrix. The $F_z \equiv H_z$ component in the general formulation in Eq. (18) can be omitted, leaving only the transverse fields $\boldsymbol{F}_t \equiv \boldsymbol{E}_t$. Likewise, only the 2×2 diagonal block of $\mathbb{G}^{\Omega}$ in the TE branch of Eq. (11c), i.e., $\frac{i}{\omega\epsilon}\mathbb{L}\mathbb{L}'$, survives. For isotropic scatterers $\boldsymbol{\alpha} = \alpha\mathbf{I}_2$ where α is a scalar and $\mathbf{I}_2$ is the 2×2 identity, and for circular cross section we have $\alpha = -8ib_1/(\omega\mu_0)$ where b_1 is the Mie series expansion coefficient of the first-order cylindrical harmonic function $H_1^{(1)}(k_0n_s\rho)\cos\theta$ in the expansion of the scattered magnetic field.

We use this formulation to test the response of the rotating array shown in Fig. 6(a), under TE excitation. For a fair comparison, the exciting source is a $\hat{z}$-directed magnetic line source at the origin, with $\lambda = 1$ μm, thus generating an essentially isotropic H_z. The corresponding $\boldsymbol{E}_t^i$ for each of the cylinders is shown in Fig. 13, as derived in Appendix C. For a reference, the currents obtained from the reduced polarizability theory are compared to an exact full-wave numerical solution based on the multifilaments method, as in the TM example. Since an integral equation of the form of Eq. (21) is not available in TE, we didnot pursue a volumetric MoM solution. The results are shown in Fig. 14. There is an excellent agreement between the methods.

Note that the rotation-induced fluctuations of $|\boldsymbol{I}_n|$ in the TE case are orders of magnitude smaller than in the TM case; they are below the graphical resolution of Fig. 14 but can be observed by zooming in. Furthermore, a close examination of the results reveals that $\boldsymbol{I}_n$ change direction monotonically as a function of Ω as seen in Figs. 14(c) and 14(d). This effect,

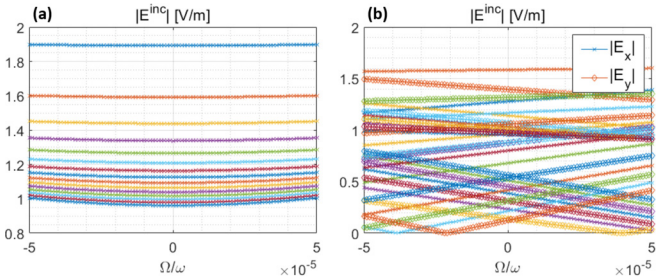

FIG. 13. The incident electric field at each of the cylinders, for the array in Fig. 6(a) in the TE case. (a) $|\boldsymbol{E}_t^i|$. (b) Its transverse components.

however, is merely induced by the change of strength and direction of the *incident* electric field $\boldsymbol{E}_t^i$ as a function of Ω; see Fig. 13. This is also the reason for the apparent slight increase of the currents at higher rotation rates. Hence, fluctuations of $\boldsymbol{I}_n$ as a function of Ω due to the array TE-*internal dynamics*, are significantly smaller compared to those for the TM case.

We have observed the same dynamics in more simulations and with other arrays; the rotation sensitivity of the TE case is generally inferior to that of the TM case. An explanation of the physics behind this phenomenon, that is consistent with the picture of excitation of Sagnac loops in the particle array and their mutual interferences as described in points #1 and #2 in Sec. III B, is schematized in Fig. 15. In TM, the polarization current excited in a scatterer is $\hat{z}$ directed hence it radiates isotropically in the (x, y) plane, maximizing the potential for excitation of Sagnac loops. In the TE case the polarization current is parallel to the (x, y) plane, thus possessing a non-isotropic radiation pattern in that plane, that maximizes at the

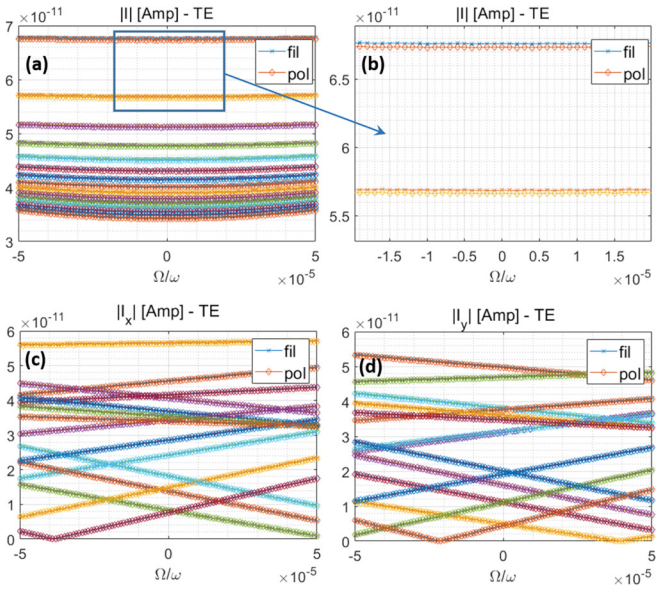

FIG. 14. The polarization current for the same array as in Fig. 6(a), but for TE excitation. (a) $|\boldsymbol{I}_n|$. (b) Zoom into the selected domain. The relative vertical scales are the same as the corresponding graphs in Fig. 6. The rotation-induced fluctuations in the response currents are orders of magnitude weaker than those for TM excitations. (c), (d) The polarization current x, y components.

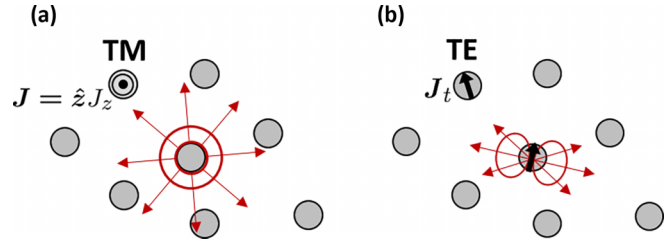

FIG. 15. Potential excitation of Sagnac loops. (a) The TM case. The polarizarion current is normal to the (x, y) plane, thus each scatterer radiates isotropically in the plane and excites all its neighbors. (b) The TE case. The polarization current is parallel to the (x, y) plane and radiates as a short dipole that possesses a selective radiation pattern. Consequently, less neighbors are excited.

broadside direction, and nullifies in end fire; a sequence of broadside scatterings cannot close a loop. Then the number of Sagnac loops that can be excited and their excitation intensity are reduced. We note that this phenomenon is not idiosyncratic to the two-dimensionality of our system. The picture described in Fig. 15 holds also when the structure is finite in the $\hat{z}$ direction. The TM excitation with respect to the rotation plane, would possess a superior sensitivity to rotation also in full 3D structures.

V. CONCLUSIONS

We developed a 2D theory governing the rest-frame electrodynamics of rotating scaterrers and particle arrays. Specifically, a formulation governing the scattering from a rotating dielectric structure of arbitrary shape and geometry, that holds in the rotating structure rest frame $\mathcal{R}^{\Omega}$ is developed and applied to electrically small scatterers. Then a polarizability theory and discrete dipole approximations are developed and introduced in Eqs. (19)–(20b). The formulation is used to study the internal dynamics of rotating scatterers and arrays. The TM polarizability matrix $\boldsymbol{\alpha}$ of dielectric cylinders of arbitrary cross section is presented, and the rotation-induced footprint is studied in the limit of electrically small cross-section. Rotation modifies the conventional entries of $\boldsymbol{\alpha}$, as well as introduces new off-diagonal terms, all depend formally on Ω and on the distance from the rotation axis $\boldsymbol{\rho}_c$ as shown in Figs. 3–5. However, within the range of parameter shown, the rotation footprint on $\boldsymbol{\alpha}$ is extremely small. Thus, we show that the conventional polarizability of $\mathcal{R}^0$ problem (no-rotation) can be used where the effect of rotation is manifested via the inter-particle propagations presented by the appropriate Green's function G^{Ω}, as expressed by Eq. (22). A comparison of Eq. (22) with rigorous numerical simulations is provided—see Fig. 6—and it supports this conclusion. Then, using this formulation the rotation-induced footprint on the array response and the governing physical mechanisms are explored. In the regime of parameters studied, it is shown that this footprint is dominated by the interference of the large number of Sagnac loops excited in the array. The array dynamics possesses unique properties such as invariance of the currents magnitude with respect to the distance from the rotation axis, while its relative phases carry information about this distance; the phase is linear with Ω, and with the rotation

axis shift, as predicted in Eq. (24c). Unlike the conventional Sagnac effect that is independent of the background medium, the rotation-induced changes of the polarization current are sensitive to the background dielectric constant.

A preliminary study of the rotation-induced footprint on the collective properties of a finite-size PhC array of dielectric cylinders with square periodicity is also provided. In the corresponding $\mathcal{R}^0$ problem, such arrays are reciprocal and possess a stop-band at a frequency regime that lies in the vicinity of Bragg condition. We show that the corresponding $\mathcal{R}^\Omega$ problem possesses a strong nonreciprocity. The transmission S_{ij} from a point P_i to point P_j satisfies $S_{ji}(\Omega) \neq S_{ij}(\Omega) = S_{ji}(-\Omega)$, as shown in Fig. 11. Furthermore, for specific point pairs determined by the structure's reflection symmetries lines, the dependence on Ω disappears as well as the nonreciprocity of S_{ij}, where it satisfies $S_{ij}(\Omega) = S_{ji}(\Omega) = S_{ij}(0)\,\forall\,\Omega$, as shown in Figs. 11 and 12.

Finally, sensitivities to rotation of TE and TM polarizations are studied and contrasted.

APPENDIX A: PDE GOVERNING NONHOMOGENOUS 2D THEORY

We define the transverse operator $\nabla_t = \hat{\boldsymbol{x}}\partial_x + \hat{\boldsymbol{y}}\partial_y$. Likewise, any vector can be decomposed into its transverse and z-directed components; e.g., $\boldsymbol{E} = \boldsymbol{E}_t + \hat{\boldsymbol{z}}E_z$. Then

$$\nabla \times \boldsymbol{E} = \nabla_t \times \boldsymbol{E}_t + \nabla_t \times \hat{\boldsymbol{z}}E_z + \partial_z \hat{\boldsymbol{z}} \times \boldsymbol{E}_t. \tag{A1}$$

Since we deal with z-independent problem the last term vanishes. By applying Eq. (A1) to ME with the constitutive relations in Eqs. (1a) and (1b), one can separate Faraday and Amper laws into their transverse and z-directed components. The results are

$$\hat{\boldsymbol{z}}: \quad \nabla_t \times \boldsymbol{E}_t = i\omega\mu\hat{\boldsymbol{z}}H_z - i\frac{\omega\Omega}{c^2}\rho\hat{\boldsymbol{z}}E_\rho - \hat{\boldsymbol{z}}J_z^{\mathrm{M}}, \tag{A2a}$$

$$\hat{\boldsymbol{t}}: \quad \nabla_t \times \hat{\boldsymbol{z}}E_z = i\omega\mu\boldsymbol{H}_t + i\frac{\omega\Omega}{c^2}\boldsymbol{\rho}E_z - \boldsymbol{J}_t^{\mathrm{M}} \tag{A2b}$$

for Faraday law, and

$$\hat{\boldsymbol{z}}: \quad \nabla_t \times \boldsymbol{H}_t = -i\omega\epsilon\hat{\boldsymbol{z}}E_z - i\frac{\omega\Omega}{c^2}\rho\hat{\boldsymbol{z}}H_\rho + \hat{\boldsymbol{z}}J_z^{\mathrm{E}}, \tag{A2c}$$

$$\hat{\boldsymbol{t}}: \quad \nabla_t \times \hat{\boldsymbol{z}}H_z = -i\omega\epsilon\boldsymbol{E}_t + i\frac{\omega\Omega}{c^2}\boldsymbol{\rho}H_z + \boldsymbol{J}_t^{\mathrm{E}} \tag{A2d}$$

for Amper law. In the above $\boldsymbol{J}^{\mathrm{E}}, \boldsymbol{J}^{\mathrm{M}}$ are the electric and magnetic current densities, respectively. It is seen that the equations above can be separated to two independent sets of fields and sources. The fields $H_z, \boldsymbol{E}_t$ with the currents $J_z^{\mathrm{M}}, \boldsymbol{J}_t^{\mathrm{E}}$ appear only in Eq. (A2a) and Eq. (A2d)—the TE set. The fields $E_z, \boldsymbol{H}_t$ with the currents $J_z^{\mathrm{E}}, \boldsymbol{J}_t^{\mathrm{M}}$ appear only in Eq. (A2b) and Eq. (A2c)—the TM set.

We develop first the TE set. From Eq. (A2d) we have

$$\boldsymbol{E}_t = \frac{i}{\omega\epsilon}\left(\nabla_t \times \hat{\boldsymbol{z}}H_z - i\frac{\omega\Omega}{c^2}\boldsymbol{\rho}H_z - \boldsymbol{J}_t^{\mathrm{E}}\right) \tag{A3}$$

substituting to Eq. (A2a), and rearranging we obtain

$$\epsilon_r\nabla_t \cdot \frac{1}{\epsilon_r}\nabla_t H_z + k_0^2\tilde{n}^2 H_z + i\frac{\omega\Omega}{c^2}\left(\partial_\theta + \epsilon\,\partial_\theta\frac{1}{\epsilon}\right)H_z = S^{\mathrm{TE}}, \tag{A4a}$$

where

$$\tilde{n}^2 = \epsilon_r(\boldsymbol{\rho})\mu_r(\boldsymbol{\rho}) + (\Omega\rho/c)^2 \tag{A4b}$$

and

$$S^{\mathrm{TE}} = -i\omega\epsilon J_z^{\mathrm{M}} + i\frac{\omega\Omega}{c^2}\boldsymbol{\rho}\cdot\boldsymbol{J}_t^{\mathrm{E}} - \hat{\boldsymbol{z}}\cdot\epsilon\nabla_t \times \frac{1}{\epsilon}\boldsymbol{J}_t^{\mathrm{E}}. \tag{A4c}$$

In the above we used the identities $\hat{\boldsymbol{\rho}}\cdot(\nabla_t \times \hat{\boldsymbol{z}}u) = \rho^{-1}\partial_\theta u$ and $\nabla_t \times (p\nabla_t \times \hat{\boldsymbol{z}}u) = -\hat{\boldsymbol{z}}\nabla_t\cdot(p\nabla_t u)$ for any scalar fields p, u. Up to first-order terms in Ω Eqs. (A3)–(A4c) are identical to the TE set in Eqs. (2)–(3b) of the main text. The governing equations for the TM case are obtained similarly.

APPENDIX B: BOUNDARY AND CONTINUITY CONDITIONS

The boundary or continuity conditions (BCs) for the tangential $\boldsymbol{E}$ and $\boldsymbol{H}$ are the same as in $\mathcal{R}^0$ problem, since ME do not change their structure. Thus,

$$\hat{\boldsymbol{n}} \times (\boldsymbol{E}_1 - \boldsymbol{E}_2) = \boldsymbol{0}, \tag{B1a}$$

$$\hat{\boldsymbol{n}} \times (\boldsymbol{H}_1 - \boldsymbol{H}_2) = \boldsymbol{K}_{\mathrm{f}}, \tag{B1b}$$

where $\boldsymbol{K}_{\mathrm{f}}$ is the surface density of the free electric current. Likewise, the *normal* components of $\boldsymbol{D}$ and $\boldsymbol{B}$ satisfy the same BCs as in $\mathcal{R}^0$ problem,

$$\hat{\boldsymbol{n}}\cdot(\boldsymbol{D}_1 - \boldsymbol{D}_2) = \eta_{\mathrm{f}}, \tag{B2a}$$

$$\hat{\boldsymbol{n}}\cdot(\boldsymbol{B}_1 - \boldsymbol{B}_2) = 0, \tag{B2b}$$

where η_{f} is the surface density of the free electric charge. However, when the latter BCs are written in terms of the normal $\boldsymbol{E}$ and $\boldsymbol{H}$ (instead of normal $\boldsymbol{D}, \boldsymbol{B}$) they take on a different form and carry an explicit dependence on Ω. We substitute the constitutive relations of Eqs. (1a) and (1b) into the BCs for the normal fields. Now recall that $\boldsymbol{\Omega} = \hat{\boldsymbol{z}}\Omega$, thus $(\boldsymbol{\Omega}\times\boldsymbol{r})\times\boldsymbol{H} = \Omega\rho\hat{\boldsymbol{\theta}}\times\boldsymbol{H}$. Then use $\hat{\boldsymbol{n}}\cdot(\hat{\boldsymbol{\theta}}\times\boldsymbol{H}) = -\hat{\boldsymbol{\theta}}\cdot(\hat{\boldsymbol{n}}\times\boldsymbol{H})$, and apply the same procedure for $(\boldsymbol{\Omega}\times\boldsymbol{r})\times\boldsymbol{E}$. Finally make use of the tangential BC in Eqs. (B1a) and (B1b). We end up with

$$\hat{\boldsymbol{n}}\cdot(\epsilon_1\boldsymbol{E}_1 - \epsilon_2\boldsymbol{E}_2) = \eta_{\mathrm{f}} - c^{-2}\Omega\rho\hat{\boldsymbol{\theta}}\cdot\boldsymbol{K}_{\mathrm{f}}, \tag{B3a}$$

$$\hat{\boldsymbol{n}}\cdot(\mu_1\boldsymbol{H}_1 - \mu_2\boldsymbol{H}_2) = 0. \tag{B3b}$$

This is the set used in the main text.

APPENDIX C: TM (TE) FIELDS DUE TO I_z^{E} (I_z^{M})

For $\hat{\boldsymbol{z}}$-directed electric current, the excited field is of TM polarization. For the current J_z^{E} of Eq. (9b) the electric and magnetic fields are given by

$$\frac{E_z}{I_z^{\mathrm{E}}} = -i\omega\mu G^\Omega(\boldsymbol{\rho}, \boldsymbol{\rho}'), \tag{C1a}$$

and using Eq. (4a)

$$\begin{aligned}\frac{\boldsymbol{H}_t}{I_z^{\mathrm{E}}} = {}& \frac{i}{4}\frac{k_0 n}{R}[\hat{\boldsymbol{x}}(y-y') - \hat{\boldsymbol{y}}(x-x')] \\ & \times H_1^{(1)}(k_0 nR)e^{ik_0^2\bar{\Omega}\hat{\boldsymbol{z}}\cdot(\boldsymbol{\rho}'\times\boldsymbol{\rho})} \\ & + i\bar{\Omega}k_0^2(\boldsymbol{\rho}-\boldsymbol{\rho}')G^\Omega(\boldsymbol{\rho}, \boldsymbol{\rho}'),\end{aligned} \tag{C1b}$$

where $G^\Omega(\boldsymbol{\rho}, \boldsymbol{\rho}')$ is given in Eqs. (7a) and (7b), $\boldsymbol{\rho} - \boldsymbol{\rho}' = \hat{\boldsymbol{x}}(x-x') + \hat{\boldsymbol{y}}(y-y')$ and $R = |\boldsymbol{\rho} - \boldsymbol{\rho}'|$. It is interesting to

note that $|E_z|$ is not affected by rotation, while $\boldsymbol{H}_t$ changes its magnitude and direction as a function of Ω.

The TE fields due to $\hat{\boldsymbol{z}}$-directed magnetic current are obtained symmetrically by $\epsilon \leftrightarrow \mu, \boldsymbol{E} \to \boldsymbol{H}, \boldsymbol{H} \to -\boldsymbol{E}$.

APPENDIX D: DERIVATION OF $\sigma_{zz}^{\mathrm{TM}}, \boldsymbol{\sigma}_{zt}^{\mathrm{TM}}$

Our starting point is the integral equation (21). Since the scatterer is electrically small $E_z(\boldsymbol{\rho}')$ is approximately uniform within $A(\boldsymbol{\rho}_c)$, while $G^{\Omega}(\boldsymbol{\rho}, \boldsymbol{\rho}')$ is singular at $\boldsymbol{\rho}' = \boldsymbol{\rho}$. Thus, Eq. (21) can be approximated by

$$E_z(\boldsymbol{\rho}) \approx E_z^i(\boldsymbol{\rho}) + E_z(\boldsymbol{\rho}) k_0^2 C \int_{A(\boldsymbol{\rho}_c)} G^{\Omega}(\boldsymbol{\rho}, \boldsymbol{\rho}') ds'. \tag{D1}$$

The local spatial variations of E_z^i within the scatterer cross section are effectively expressed via the corresponding local $\boldsymbol{H}_t$. To correctly capture the rotation footprint on E_z and hence on $\sigma_{zz}^{\mathrm{TM}}$ and $\boldsymbol{\sigma}_{zt}^{\mathrm{TM}}$, we endeavor to establish an $\bar{\Omega}$-induced pointwise connection between $E_z^i(\boldsymbol{\rho})$ and $E_z^i(\boldsymbol{\rho}_c), \boldsymbol{H}_t^i(\boldsymbol{\rho}_c)$. Toward this end, we first expand

$$E_z^i(\boldsymbol{\rho}) \simeq E_z^i(\boldsymbol{\rho}_c) + \boldsymbol{\nabla}_t E_z^i(\boldsymbol{\rho}_c) \cdot (\boldsymbol{\rho} - \boldsymbol{\rho}_c), \tag{D2a}$$

where $\boldsymbol{\nabla}_t E_z(\boldsymbol{\rho})$ is extracted from Eq. (4a),

$$\boldsymbol{\nabla}_t E_z^i(\boldsymbol{\rho}_c) = i\omega\mu \hat{\boldsymbol{z}} \times \boldsymbol{H}_t^i(\boldsymbol{\rho}_c) + i\bar{\Omega} k_0^2 (\hat{\boldsymbol{z}} \times \boldsymbol{\rho}_c) E_z^i(\boldsymbol{\rho}_c), \tag{D2b}$$

and where we have used the identities $\boldsymbol{\nabla}_t \times \hat{\boldsymbol{z}} E_z = -\hat{\boldsymbol{z}} \times \boldsymbol{\nabla}_t E_z$ and $\hat{\boldsymbol{z}} \times \hat{\boldsymbol{z}} \times \boldsymbol{\nabla}_t E_z = -\boldsymbol{\nabla}_t E_z$. Then, the expansion of $E_z^i(\boldsymbol{\rho})$ in Eq. (D2a) can be written as

$$\begin{aligned} E_z^i(\boldsymbol{\rho}) \simeq & \left[1 + i\bar{\Omega} k_0^2 \rho_c \hat{\boldsymbol{\theta}}_c \cdot (\boldsymbol{\rho} - \boldsymbol{\rho}_c)\right] E_z^i(\boldsymbol{\rho}_c) \\ & - i\omega\mu [\hat{\boldsymbol{z}} \times (\boldsymbol{\rho} - \boldsymbol{\rho}_c)] \cdot \boldsymbol{H}_t^i(\boldsymbol{\rho}_c), \end{aligned} \tag{D2c}$$

where $\hat{\boldsymbol{\theta}}_c = \hat{\boldsymbol{z}} \times \hat{\boldsymbol{\rho}}_c$ with $\hat{\boldsymbol{\rho}}_c = \boldsymbol{\rho}_c / \rho_c$ (see Fig. 2), and where we used the identity $[\hat{\boldsymbol{z}} \times \boldsymbol{H}_t^i(\boldsymbol{\rho}_c)] \cdot (\boldsymbol{\rho} - \boldsymbol{\rho}_c) = -[\hat{\boldsymbol{z}} \times (\boldsymbol{\rho} - \boldsymbol{\rho}_c)] \cdot \boldsymbol{H}_t^i(\boldsymbol{\rho}_c)$. By substituting Eq. (D2c) in Eq. (D1), extracting $E_z(\boldsymbol{\rho})$ and integrating over the scatterer cross section, we get for the spatially averaged E_z in the scatterer,

$$\bar{E}_z = \sigma_{zz}^{\mathrm{TM}}(\Omega, \boldsymbol{\rho}_c) E_z^i(\boldsymbol{\rho}_c) + \boldsymbol{\sigma}_{zt}^{\mathrm{TM}}(\Omega, \boldsymbol{\rho}_c) \cdot \boldsymbol{H}_t^i(\boldsymbol{\rho}_c), \tag{D3}$$

where

$$\sigma_{zz}^{\mathrm{TM}}(\Omega, \boldsymbol{\rho}_c) = \frac{1}{A} \int_{A(\boldsymbol{\rho}_c)} \frac{1 + i\bar{\Omega} k_0^2 \rho_c \hat{\boldsymbol{\theta}}_c \cdot (\boldsymbol{\rho} - \boldsymbol{\rho}_c)}{1 - \psi(\Omega, \boldsymbol{\rho})} ds, \tag{D4a}$$

$$\boldsymbol{\sigma}_{zt}^{\mathrm{TM}}(\Omega, \boldsymbol{\rho}_c) = -i \frac{\omega\mu}{A} \int_{A(\boldsymbol{\rho}_c)} \frac{\hat{\boldsymbol{z}} \times (\boldsymbol{\rho} - \boldsymbol{\rho}_c)}{1 - \psi(\Omega, \boldsymbol{\rho})} ds, \tag{D4b}$$

and

$$\psi(\Omega, \boldsymbol{\rho}) = k_0^2 C \int_{A(\boldsymbol{\rho}_c)} G^{\Omega}(\boldsymbol{\rho}, \boldsymbol{\rho}') ds'. \tag{D4c}$$

These explicit expressions can be evaluated easily by straightforward integrations. Examples are provided in Sec. III. However, it is instructive to extract the dominant behavior of the scattering matrix in terms of power series in $\bar{\Omega}$. This behavior is of interest not only from the numerical point of view. It represents an important physical property; a second-order dependence on Ω indicates that the corresponding property is insensitive to the rotation direction, while first-order dependence indicates a sensitivity to the rotation direction. Toward this end, with $(1 - \psi)^{-1} \simeq 1 + \psi$ we write approximately

$$\begin{aligned} A\sigma_{zz}^{\mathrm{TM}} \simeq & \int_{A(\boldsymbol{\rho}_c)} \left[1 + i\bar{\Omega} k_0^2 \rho_c \hat{\boldsymbol{\theta}}_c \cdot (\boldsymbol{\rho} - \boldsymbol{\rho}_c)\right] ds \\ & + k_0^2 C \iint_{A(\boldsymbol{\rho}_c)} \left[1 + i\bar{\Omega} k_0^2 \rho_c \hat{\boldsymbol{\theta}}_c \cdot (\boldsymbol{\rho} - \boldsymbol{\rho}_c)\right] \\ & \times G^{\Omega}(\boldsymbol{\rho}, \boldsymbol{\rho}') ds' ds. \end{aligned} \tag{D5}$$

By the definition of $\boldsymbol{\rho}_c$ in Eq. (15), the second summand of the first integral does not survive the integration, hence the first integral is nothing but A. Regarding the second integral, we first note that since the structure is electrically small, and $|\bar{\Omega}| \ll 1$, we may expand

$$\begin{aligned} G^{\Omega}(\boldsymbol{\rho}, \boldsymbol{\rho}') = & G^0(\boldsymbol{\rho}, \boldsymbol{\rho}') \{1 + i\bar{\Omega} k_0^2 \hat{\boldsymbol{z}} \cdot (\boldsymbol{\rho}' \times \boldsymbol{\rho}) \\ & - \tfrac{1}{2} (\bar{\Omega} k_0^2)^2 [\hat{\boldsymbol{z}} \cdot (\boldsymbol{\rho}' \times \boldsymbol{\rho})]^2 + \cdots \}. \end{aligned} \tag{D6}$$

We further note that $\hat{\boldsymbol{\theta}}_c \cdot (\boldsymbol{\rho} - \boldsymbol{\rho}_c) = -\hat{\boldsymbol{z}} \cdot (\boldsymbol{\rho} \times \boldsymbol{\rho}_c)$ and point the similarity to the summed terms in the expansion of G^{Ω} above. Substituting the above expansion and identity into Eq. (D5) and rearranging as a power series in $\bar{\Omega}$, we obtain

$$\sigma_{zz}^{\mathrm{TM}}(\Omega, \boldsymbol{\rho}_c) \simeq \sigma_{zz}^{\mathrm{TM}}(0, \boldsymbol{0}) + \bar{\Omega}\sigma_1 + \bar{\Omega}^2 \sigma_2 + \cdots. \tag{D7}$$

We now show that the first-order term vanishes, i.e., $\sigma_1 = 0$ meaning that $\sigma_{zz}^{\mathrm{TM}}(\Omega, \boldsymbol{\rho}_c)$ is second order in Ω at most. Specifically, we have

$$\sigma_1 = ik_0^4 C A^{-1} \iint_{A(\boldsymbol{\rho}_c)} G^0(\boldsymbol{\rho}, \boldsymbol{\rho}') \hat{\boldsymbol{z}} \cdot [\boldsymbol{\rho} \times (\boldsymbol{\rho}_c - \boldsymbol{\rho}')] ds ds'. \tag{D8}$$

The vector terms in this integral can be rewritten as the sum $\hat{\boldsymbol{z}} \cdot [\boldsymbol{\rho} \times (\boldsymbol{\rho}_c - \boldsymbol{\rho}')] = \hat{\boldsymbol{z}} \cdot (\boldsymbol{\rho}' - \boldsymbol{\rho}) - \rho_c \boldsymbol{\rho} \cdot \hat{\boldsymbol{\theta}}_c$. The former does not survive the integration since both $\boldsymbol{\rho}$ and $\boldsymbol{\rho}'$ span precisely the same area, but upon exchanging $\boldsymbol{\rho}$ and $\boldsymbol{\rho}'$ the Greens function $G^0(\boldsymbol{\rho}, \boldsymbol{\rho}')$ remains invariant while $\hat{\boldsymbol{z}} \cdot (\boldsymbol{\rho}' - \boldsymbol{\rho})$ merely change sign, thus the net integration is zero. Regarding the latter term, we first note that for every function $F(x)$ the integral function $I(\boldsymbol{\rho}) = \int_A F(|\boldsymbol{\rho} - \boldsymbol{\rho}'|) ds'$ is symmetric around $\boldsymbol{\rho} = \boldsymbol{\rho}_c$, while $\boldsymbol{\rho} \cdot \hat{\boldsymbol{\theta}}_c$ is antisymmetric (for example, if $\boldsymbol{\rho}_c = \hat{\boldsymbol{x}} \rho_c$, then $\hat{\boldsymbol{\theta}}_c = \hat{\boldsymbol{y}}$ and $\boldsymbol{\rho} \cdot \hat{\boldsymbol{\theta}}_c = y$). Thus, the integration over the former term vanishes as well. Consequently, $\sigma_1 = 0$ as anticipated.

We follow essentially the same steps for $\boldsymbol{\sigma}_{zt}^{\mathrm{TM}}(\Omega, \boldsymbol{\rho}_c)$. We have

$$\begin{aligned} \boldsymbol{\sigma}_{zt}^{\mathrm{TM}} \simeq & -i \frac{\omega\mu}{A} \hat{\boldsymbol{z}} \times \int_{A(\boldsymbol{\rho}_c)} (\boldsymbol{\rho} - \boldsymbol{\rho}_c) ds \\ & - i \frac{\omega\mu}{A} k_0^2 C \hat{\boldsymbol{z}} \times \iint_{A(\boldsymbol{\rho}_c)} (\boldsymbol{\rho} - \boldsymbol{\rho}_c) G^{\Omega}(\boldsymbol{\rho}, \boldsymbol{\rho}') ds' ds. \end{aligned} \tag{D9}$$

The first integral vanishes by the definition of $\boldsymbol{\rho}_c$—see Eq. (15). Likewise, by using the expansion in Eq. (D6) for G^{Ω} in the second integral above, and recalling again Eq. (15), we are left with

$$\begin{aligned} \boldsymbol{\sigma}_{zt}^{\mathrm{TM}} \simeq & \frac{\omega\mu}{A} k_0^4 C \bar{\Omega} \hat{\boldsymbol{z}} \iint_{A(\boldsymbol{\rho}_c)} G^0(\boldsymbol{\rho}, \boldsymbol{\rho}') (\boldsymbol{\rho} - \boldsymbol{\rho}_c) \\ & \times \hat{\boldsymbol{z}} \cdot (\boldsymbol{\rho}' \times \boldsymbol{\rho}) ds' ds + \mathcal{O}(\bar{\Omega}^2) \end{aligned} \tag{D10}$$

that generally does not vanish. Hence, the leading element of $\boldsymbol{\sigma}_{zt}^{\mathrm{TM}}$ is first order in Ω. Note the term $\hat{\boldsymbol{z}} \times (\boldsymbol{\rho} - \boldsymbol{\rho}_c) = \rho\hat{\boldsymbol{\theta}} - \rho_c\hat{\boldsymbol{\theta}}_c$. For scatterers possessing reflection symmetry around the line defined by $\boldsymbol{\rho}_c$, e.g., with circular cross section, or one of their axes of symmetry is *parallel* to ρ_c, this term does not survive the integration. This leads to $\sigma_{z\theta}^{\mathrm{TM}}$ that is second order in Ω. This is schematized in Fig. 2(b). Thus, $\sigma_{z\rho}^{\mathrm{TM}}$ is first order in $\bar{\Omega}$, while $\sigma_{z\theta}^{\mathrm{TM}}$ may be first or second order in $\bar{\Omega}$, depending on the scatterer symmetries and its inclination with respect to $\boldsymbol{\rho}_c$.

APPENDIX E: EXTRACTING σ NUMERICALLY

Let $\boldsymbol{F}^i = [E_z^i(\boldsymbol{\rho}), \boldsymbol{H}_t^i(\boldsymbol{\rho})]$ be the incident electric and magnetic fields, and $\bar{E}_z$ the resulting spatially averaged electric field inside the scatterer. The latter can be obtained by solving Eq. (21) numerically using the volumetric method of moments [26] and spatially averaging the result. Then the scattering matrix $\boldsymbol{\sigma}$ formally satisfies

$$\sigma_{zz}E_z^i(\boldsymbol{\rho}_c) + \sigma_{z\rho}H_\rho^i(\boldsymbol{\rho}_c) + \sigma_{z\theta}H_\theta^i(\boldsymbol{\rho}_c) = \bar{E}_z. \tag{E1a}$$

Since the entries and their corresponding rotation footprint span over wide rage of orders, and further, in σ_{zz} it appears as an additive term of relative strength of $\mathcal{O}(10^{-7})$ compare to its base value for $\mathcal{R}^0$ problem, a numerically stable and reliable solution is challenging. To stabilize their extraction we use the following procedure. First, let us define an auxiliary quantity $\boldsymbol{\sigma}^d$ via

$$\sigma_{zz}^d E_z^i(\boldsymbol{\rho}_c) + \sigma_{z\rho}^d H_\rho^i(\boldsymbol{\rho}_c) + \sigma_{z\theta}^d H_\theta^i(\boldsymbol{\rho}_c) = \bar{E}_z - \bar{E}_z^i. \tag{E1b}$$

Once $\boldsymbol{\sigma}^d$ is obtained we approximate $\boldsymbol{\sigma} = (1, 0, 0) + \boldsymbol{\sigma}^d$. We need at least $m = 3$ independent incident fields $\boldsymbol{F}_n^i$, $n = 1, \ldots, m$ and their corresponding internal $E_{z,n}$ solutions to get m equations of the form of Eq. (E1b). However, to average over numerical inaccuracies, we use a set of $m = 8$ different incident fields, and solve the over-determined set of equations for the three unknown elements of $\boldsymbol{\sigma}^d$ in the least-square sense. These incident fields are synthesized by eight point sources of unit current located around the scatterer on two circles, four on a circle of radius 5λ at angles $0^\circ, 90^\circ, 180^\circ, 270^\circ$ and four on a 50λ circle, at the same angles. The corresponding $\boldsymbol{F}_n^i$, $n = 1, \ldots, 8$ are calculated using Eqs. (C1a) and (C1b). Finally, we note that to correctly capture the effect of the fine-details variation of E_z^i on the resulting internal field, the field solution to each of these sources is obtained by a two-step solution of Eq. (21). For each of the sources, we rewrite the incident field as the sum of its spatially averaged value and a reminder, i.e., $E_z^i(\boldsymbol{\rho}) = \bar{E}_z^i + \Delta E_z^i(\boldsymbol{\rho})$. Then we solve Eq. (21) with $E_z^i(\boldsymbol{\rho})$ replaced by each of the latter components, and sum up the corresponding solutions for the scatterer internal field $E_z(\boldsymbol{\rho})$. This field is then used in Eq. (E1b).

[1] T. Shiozawa, Phenomenological and electron-theoretical study of the electrodynamics of rotating systems, Proc. IEEE **61**, 1694 (1973).

[2] M. G. Silveirinha, Optical instabilities and spontaneous light emission by polarizable moving matter, Phys. Rev. X **4**, 031013 (2014).

[3] Y. Mazor and A. Alù, Nonreciprocal hyperbolic propagation over moving metasurfaces, Phys. Rev. B **99**, 045407 (2019).

[4] A. Manjavacas and F. J. G. de Abajo, Vacuum friction in rotating particles, Phys. Rev. Lett. **105**, 113601 (2010).

[5] Y. B. Zel'dovich, Amplification of cylindrical electromagnetic waves reflected from a rotating body, Sov. Phys. JETP **35**, 1085 (1972).

[6] S. Lannebère and M. G. Silveirinha, Wave instabilities and unidirectional light flow in a cavity with rotating walls, Phys. Rev. A **94**, 033810 (2016).

[7] B. Z. Steinberg and N. Engheta, Rest-frame quasi-static theory for rotating electromagnetic systems and circuits, Phys. Rev. B **107**, 195418 (2023).

[8] Y. B. Zel'dovich, L. V. Rozhanskii, and A. Starobinskii, Rotating bodies and electrodynamics in a rotating coordinate system, Radiophys. Quantum Electron. **29**, 761 (1986).

[9] J. V. Bladel, Electromagnetic fields in the presence of rotating bodies, Proc. IEEE **64**, 301 (1976).

[10] D. D. Zutter and D. Goethals, Scattering by a rotating dielectric sphere, IEEE Trans. Antennas Propag. **28**, 643 (1980).

[11] D. D. Zutter and D. Goethals, Scattering by a rotating conducting sphere, IEEE Trans. Antennas Propag. **32**, 95 (1984).

[12] R. Reimann, M. Doderer, E. Hebestreit, R. Diehl, M. Frimmer, D. Windey, F. Tebbenjohanns, and L. Novotny, GHz rotation of an optically trapped nanoparticle in vacuum, Phys. Rev. Lett. **121**, 033602 (2018).

[13] J. Ahn, Z. Xu, J. Bang, Y.-H. Deng, T. M. Hoang, Q. Han, R.-M. Ma, and T. Li, Optically levitated nanodumbbell torsion balance and GHz nanomechanical rotor, Phys. Rev. Lett. **121**, 033603 (2018).

[14] B. Z. Steinberg, Rotating photonic crystals: A medium for compact optical gyroscopes, Phys. Rev. E **71**, 056621 (2005).

[15] B. Z. Steinberg and A. Boag, Splitting of micro-cavity degenerate modes in rotating photonic crystals—The miniature optical gyroscopes, J. Opt. Soc. Am. B **24**, 142 (2007).

[16] E. J. Post, Sagnac effect, Rev. Mod. Phys. **39**, 475 (1967).

[17] S. Sunada and T. Harayama, Sagnac effect in resonant microcavities, Phys. Rev. A **74**, 021801(R) (2006).

[18] S. Sunada and T. Harayama, Design of resonant microcavities: Application to optical gyroscopes, Opt. Express **15**, 16245 (2007).

[19] R. Sarma, L. Ge, J. Wiersig, and H. Cao, Rotating optical microcavities with broken chiral symmetry, Phys. Rev. Lett. **114**, 053903 (2015).

[20] R. Sarma, L. Ge, and H. Cao, Optical resonances in rotating dielectric microcavities of deformed shape, J. Opt. Soc. Am. B **32**, 1736 (2015).

[21] D. Pan, H. Xu, and F. J. G. de Abajo, Circular dichroism in rotating particles, Phys. Rev. Lett. **123**, 066803 (2019).

[22] J. V. Bladel, *Electromagnetic Fields*, 2nd ed. (IEEE Press and Wiley-Interscience, New York, NY, 2007).

[23] B. Z. Steinberg, A. Shamir, and A. Boag, Two-dimensional Greens function theory for the electrodynamics of rotating medium, Phys. Rev. E **74**, 016608 (2006).

[24] C. W. Misner, K. S. Thorne, and J. A. Wheeler, *Gravitation* (Princeton University Press, Princeton, NJ, 2017).

[25] Y. Mazor and B. Z. Steinberg, Rest-frame interference in rotating structures and metamaterials, Phys. Rev. Lett. **123**, 243204 (2019).

[26] A. F. Peterson, S. L. Ray, and R. Mittra, *Computational Methods for Electromagnetics* (IEEE Press, New York, NY, 1998).

[27] Y. Leviatan and A. Boag, Analysis of electromagnetic scattering from dielectric cylinders using a multifilament current model, IEEE Trans. Antennas Propag. **35**, 1119 (1987).

[28] S. F. Liew, H. Noh, J. Trevino, L. D. Negro, and H. Cao, Localized photonic band edge modes and orbital angular momenta of light in a golden-angle spiral, Opt. Express **19**, 23631 (2011).

[29] T. Geva and B. Z. Steinberg, Rest-frame analysis of rotating metamaterials, gyroscopes, and century-old problems in number theory, Opt. Mater. Express **13**, 1870 (2023).

[30] S. Ezekiel and H. J. Arditty, Springer series in optical sciences, *Fiber-Optic Rotation Sensors* (Springer-Verlag, Berlin, 1982).